QICT: Receiver Distinguishability and the Spectral Derivation of Standard-Model Structure

Mohamed Sacha *

Posted Date: 26 May 2026

doi: 10.20944/preprints202604.0323.v5

Keywords: copy time; receiver quotient; finite spectral triple; noncommutative geometry; neutrino mixing; spectral action

 doi:10.20944/preprints202604.0323.v5

Article

QICT: Receiver Distinguishability and the Spectral Derivation of Standard-Model Structure

Mohamed Sacha

Independent Researcher, Casablanca, Morocco; sachamed@gmail.com

Abstract

This paper formulates Quantum Information Copy Time (QICT) as a relational receiver–spectral closure for quantum information copy time. A receiver is not an observer postulate; it is a finite operational boundary, represented by a quotient algebra and by projectors selecting the degrees of freedom that can be distinguished at that boundary. Imposing receiver distinguishability, fixed-point-free copy opposition, oriented endpoint transport and first-order opposite locality selects the finite algebra $\mathcal{A}_F \simeq \mathbb{C} \oplus \mathbb{H} \oplus M_3(\mathbb{C})$ and the primitive endpoint denominator $q = 14$. The neutral Takagi extension gives $q_\nu = 21$, $\theta_{13}^{\mathrm{PMNS}} = \pi/21$, a negative leptonic Jarlskog branch and the mass sum $\sum_i m_i = 0.072810131\,\mathrm{eV}$. Independent finite-channel contractions generate CKM, electroweak and receiver-reconstruction ledgers with explicit exclusion criteria. Unlike grand-unified or string-theoretic embeddings, the construction does not begin from a simple gauge group, extra dimensions or compactification data; it begins from a finite receiver quotient and derives the internal algebra before numerical comparison. A new prospective signature is predicted: a receiver-null boundary-to-Majorana endpoint echo with quadratic onset, phase maxima $\pi/21 + 2\pi a/3$, and period ratio $3/2$. The online resources provide derivations, finite traces, determinant and residue calculations, numerical simulations, and audit code.

Keywords: copy time; receiver quotient; finite spectral triple; noncommutative geometry; neutrino mixing; spectral action

---

1. Introduction

The operational copy-time programme begins from a minimal question: when does a receiver acquire enough information to distinguish two source preparations? In isolation this question defines an operational time; the finite closure below supplies the particle-physics representation. A finite extension must therefore specify which conclusions are receiver-operational, which are spectral, and which require a closure tying the two descriptions together. The construction developed here supplies that closure. The receiver layer gives validator selection, shell geometry, six-cell transport, compact exchange covariance, exact two-channel dynamics, visible and null receiver branches, spectral inversion, hydrodynamic limits, gap-length reconstruction, and platform-independent falsification. The spectral layer gives the finite observable algebra, real structure, chiral module, unimodular gauge quotient, finite spectral action, endpoint holonomies, flavour matrices, and the neutral Majorana sector.

The central requirement is mutual constraint. Receiver data determine an observable quotient and a normal form. The finite spectral construction supplies the internal representation, and the primitive closure ties the two structures to a common receiver-visible quotient. The primitive closure principle imposes both requirements at once. A finite degree of freedom is retained exactly when it survives receiver quotient, fixed-point-free copy opposition, oriented endpoint transport, and first-order opposite locality. Quotient-null summands and reducible multiplicities are removed. From this single principle the six-cell contour, two-fold opposition, three-endpoint quotient, continuous phase carrier, pseudoreal opposition fibre, and irreducible endpoint shield are obtained as consequences.

 doi:10.20944/preprints202604.0323.v5

The article develops the receiver construction, finite spectral construction, gauge and matter completion, flavour sector, neutral generator, finite predictions, threshold predictions, reconstructions, and validation observables, and falsification protocol. The supplementary information gives the finite block classification, endpoint denominator proof, holographic ground-denominator proof, Morita-rigidity audit for the finite trace constants, receiver propagator formulae, hydrodynamic expansion, anomaly tables, hypercharge solution, neutral matrix entries, audit scripts, and supplementary data inventory.

The online resources are part of the logical chain of the submission. Online Resource 1 contains the extended supplementary information for finite closure, receiver reconstruction, anomaly cancellation, precision ledgers, and validation protocols. Online Resource 2 gives the complete spectral derivation of the Takagi fold and neutral mass constants, including the audit submodule, channel operator, projectors, boundary determinant, quaternionic endpoint residue, primitive angle theorem, and reproduction script. Online Resource 3 gives the complete prediction ledger and the prospective receiver-null endpoint echo. Online Resource 4 contains code and machine-readable audit data.

Relational Status of the Receiver

The term receiver is used in a strictly mathematical sense. It does not denote a conscious observer, a measurement subject, or a metaphysical primitive. It denotes an operational boundary specified by a family of distinguishability amplitudes, a receiver-null ideal, and the quotient algebra visible after that ideal is removed. This use is compatible with relational approaches to quantum theory, where physical content is assigned to relations between systems rather than to absolute state descriptions [16,17]. In the present construction the relation is made algebraic: the receiver selects a quotient, the quotient selects finite channels, and only those channels may enter the primitive spectral module. All subsequent numerical claims are therefore claims about the finite receiver–spectral pair, not about an observer-dependent ontology.

Relation to String-Theoretic and Grand-Unified Strategies

The construction differs from two standard unification strategies. String theory starts from extended fundamental objects and typically requires additional geometric or compactification data before a four-dimensional low-energy sector is specified [19,20]. Grand-unified theories embed the Standard Model gauge group into a larger simple group, with familiar consequences for representation unification and high-scale symmetry breaking [18]. The receiver–spectral closure follows a different route. It does not assume a simple unifying gauge group, supersymmetry, a compactification manifold, or a landscape of vacua. The starting object is the finite receiver quotient; the internal algebra is the direct sum $\mathbb{C} \oplus \mathbb{H} \oplus M_3(\mathbb{C})$, selected by phase, pseudoreal opposition and endpoint irreducibility. The resulting theory is narrower in ultraviolet ambition than a full theory of quantum gravity, but sharper in its finite audit trail: the endpoint denominator, trace constants, neutral ladder, CKM/electroweak ledgers and receiver-null echo have explicit projector, determinant, residue or regression tests. The appropriate comparison is therefore not replacement of string theory or GUTs, but a distinct finite-operational route to internal structure and falsifiable receiver signatures.

Structural Answers Fixed by the Closure

The construction is organized so that the three standard structural questions are answered before numerical comparison. The number of generations is the cardinality of the primitive endpoint quotient: the smallest receiver contour with fixed-point-free copy opposition and oriented nontrivial endpoint transport is C_6, and quotienting by opposition gives $C_6/I \simeq \mathbb{Z}_3$. The internal blocks are the three primitive carriers required by receiver-visible phase, copy opposition and endpoint transport: $\mathbb{C}$, $\mathbb{H}$, and the irreducible clock-shift shield $M_3(\mathbb{C})$. The numerical constants used in the flavour and electroweak precision sector are not fitted parameters; they are trace invariants of spectral projectors of the global finite tuple $(D_F, J, \Gamma, \rho(\mathcal{A}_F))$. The endpoint denominator is the unique primitive holographic

 doi:10.20944/preprints202604.0323.v5

ground denominator; higher admissible denominators are excited lifts with larger boundary entropy and are not primitive sectors.

2. Primitive Copy Time and Receiver Quotient

Let S and R denote disjoint source and receiver regions. The copy time at discrimination threshold $\eta \in (0,1)$ is

$$\tau_{\mathrm{copy}}(S \to R;\eta) = \inf\left\{ t \geq 0 : \frac{1}{2}\|\rho_{+,R}(t) - \rho_{-,R}(t)\|_1 \geq \eta \right\}. \tag{1}$$

The closure constructs the minimal finite algebra that remains visible after the receiver quotient associated with (1). Let $\mathcal{A}_0$ be a finite involutive algebra acting on $\mathcal{H}$, and let $\mathcal{R}$ be the family of receiver sesquilinear amplitudes closed under preparation, adjoint reversal, and endpoint relabelling. The receiver-null ideal is

$$\mathcal{N}_R = \{a \in \mathcal{A}_0 : \Phi(x^* a y) = 0 \text{ for all } \Phi \in \mathcal{R} \text{ and all receiver preparations } x, y\}. \tag{2}$$

The observable algebra is $\mathcal{A}_R = \mathcal{A}_0/\mathcal{N}_R$. The quotient is imposed before finite classification. This ordering is essential: visible algebraic structure is assigned only to degrees of freedom with nonzero receiver amplitudes.

Definition 2.1 (Primitive receiver–spectral closure)**.** *A finite degree of freedom is primitive when it satisfies four conditions: receiver distinguishability in $\mathcal{A}_R$; compatibility with a fixed-point-free copy opposition; compatibility with an oriented endpoint quotient; and first-order locality relative to the opposite representation. The primitive algebra is obtained after removing quotient-null summands and reducible multiplicities.*

The minimal finite contour carrying fixed-point-free opposition and three endpoint classes is $C_6 = \mathbb{Z}/6\mathbb{Z}$ with involution $I(j) = j + 3$. The quotient C_6/I has three endpoint classes. A three-cycle has no fixed-point-free opposition, while a four-cycle has no faithful three-endpoint quotient. Hence six cells are forced by the coexistence of two-copy opposition and three-endpoint orientation.

Theorem 2.2 (Three endpoint classes)**.** *Under receiver distinguishability, fixed-point-free copy opposition, oriented endpoint transport and primitive boundary saturation, the endpoint quotient has exactly three classes.*

Proof. Fixed-point-free opposition requires an even contour. A two-cell contour carries opposition but has a one-class quotient, and a four-cell contour has a two-class quotient. Neither can carry fixed, forward and inverse endpoint actions simultaneously. The next even contour is C_6, whose opposition quotient has three classes. Any larger even contour carrying the same three endpoint actions contains additional receiver-boundary cells not required by the quotient. Primitive boundary saturation removes those redundant cells. Thus $|C_6/I| = 3$ is forced. □

 doi:10.20944/preprints202604.0323.v5

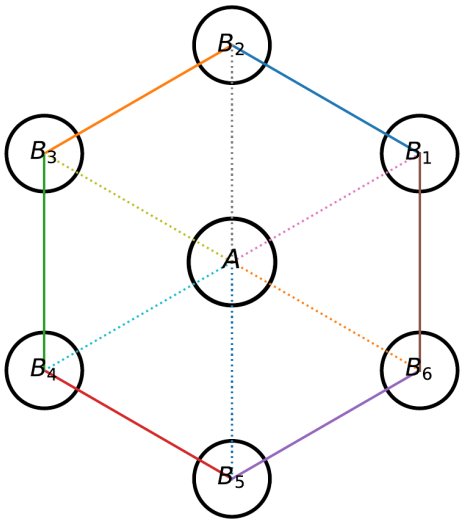

Figure 1. Receiver-side validator shell and certified six-cell contour. The contour is the minimal local support carrying both fixed-point-free opposition and a three-endpoint quotient.

3. Validator Selection and Shell Geometry

The receiver closure begins with a validator. On a homogeneous locally finite substrate X, define

$$\mathcal{J}_x[\rho] = \tau_{\mathrm{ret}}(x;\rho) + \lambda \mathcal{R}_x[\rho], \qquad \lambda > 0, \tag{3}$$

where τ_{ret} is the first certified return time and $\mathcal{R}_x$ is the receiver residual. A validator is a minimizer of $\mathcal{J}_x$. If the substrate dynamics is equivariant under a group G, then the minimizer set is carried into itself by G. Perturbative loading or preparation defects split degeneracies generically because the linearized differences $\delta\mathcal{J}_x - \delta\mathcal{J}_y$ are non-zero on the complement of a finite union of codimension-one hyperplanes. Thus the validator is equivariantly selected on homogeneous substrates and generically unique under small symmetry-breaking preparations.

The receiver shell is codimension one relative to the local bulk. Six cells are the smallest local cycle supporting: nearest-neighbour return, an antipodal copy map, and three endpoint classes. Nonlocal chords can shorten global distances, while the local nearest-neighbour contour remains the certified support for return auditing. The support of the linear receiver theory is therefore not an arbitrary hexagon; it is the minimal certified contour compatible with copy opposition and endpoint transport.

4. Gauge-Covariant Exchange and Chiral Spoke Sector

Local compact covariance acts on Hermitian fibres. A triplet Hermitian fibre has automorphism group $U(3)$ before determinant reduction; a doublet opposition fibre has $U(2)$; a central phase line has $U(1)$. The ring sector transports colour-phase exchange on the endpoint shield. The spoke sector couples opposite sheets and supplies the chiral doublet. The primitive direct-sum algebra obtained below has unitary group

$$U(1) \times SU(2) \times U(3), \tag{4}$$

with unimodular reduction to

$$S(U(1) \times U(2) \times U(3)) \simeq \frac{U(1) \times SU(2) \times SU(3)}{\Gamma}, \tag{5}$$

where Γ is the finite central overlap. In the minimal chiral one-family module, gauge-invariant Yukawa couplings and local anomaly cancellation give the familiar hypercharge pattern. Explicitly, writing

$$Q_L : (3,2)_{1/6}, \quad u_R : (3,1)_{2/3}, \quad d_R : (3,1)_{-1/3}, \quad L_L : (1,2)_{-1/2}, \quad e_R : (1,1)_{-1}, \tag{6}$$

 doi:10.20944/preprints202604.0323.v5

with optional $\nu_R : (1,1)_0$, the anomaly sums satisfy

$$\begin{aligned} [SU(3)]^2U(1): &\quad 2Y_Q - Y_u - Y_d = 0, \\ [SU(2)]^2U(1): &\quad 3Y_Q + Y_L = 0, \\ [U(1)]^3: &\quad 6Y_Q^3 - 3Y_u^3 - 3Y_d^3 + 2Y_L^3 - Y_e^3 = 0, \\ \mathrm{grav}^2U(1): &\quad 6Y_Q - 3Y_u - 3Y_d + 2Y_L - Y_e = 0. \end{aligned} \tag{7}$$

The solution is unique up to normalization once the Yukawa terms $\bar{Q}_L \tilde{H} u_R$, $\bar{Q}_L H d_R$, and $\bar{L}_L H e_R$ are required. The supplementary information gives the linear solution and the cubic check.

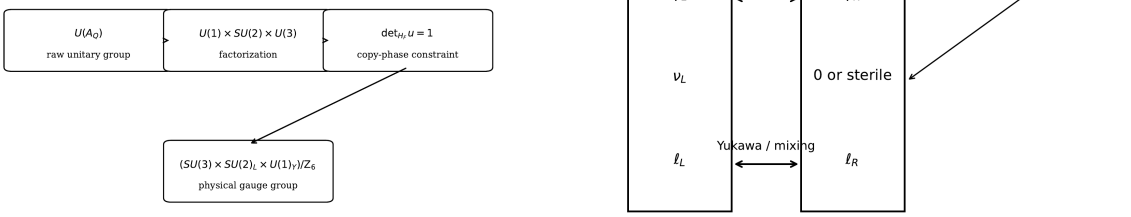

(**a**) Unimodular reduction. (**b**) Chiral module.

Figure 2. Gauge quotient and chiral matter completion arising from the finite receiver–spectral closure.

5. Exact Two-Channel Receiver Dynamics

The low-momentum receiver-accessible sector reduces to a real two-channel Hermitian generator

$$H_R(k) = (\mu + \kappa k^2)\mathbf{1}_2 + (m + \nu k^2)\sigma_1 + \Delta\sigma_3 + O(k^4). \tag{8}$$

The eigenvalues are

$$E_\pm(k) = \mu + \kappa k^2 \pm \sqrt{\Delta^2 + (m + \nu k^2)^2} + O(k^4). \tag{9}$$

The exact propagator of the quadratic two-channel generator is

$$e^{-itH_R(k)} = e^{-it(\mu+\kappa k^2)}\left[\cos(t\Omega_k)\mathbf{1}_2 - i\frac{\sin(t\Omega_k)}{\Omega_k}\Big((m + \nu k^2)\sigma_1 + \Delta\sigma_3\Big)\right], \tag{10}$$

where $\Omega_k = \sqrt{\Delta^2 + (m + \nu k^2)^2}$. For a chirality-selective receiver projector $P_+ = |+\rangle\langle+|$, the receiver-visible leakage from the opposite channel is

$$\mathcal{L}_{-\to+}(t,k) = \frac{(m + \nu k^2)^2}{\Omega_k^2}\sin^2(t\Omega_k). \tag{11}$$

At $m = 0$, the receiver-null branch is invariant. For small m, the first visible onset is quadratic in m and provides a robust curvature target.

Theorem 5.1 (Algebraic receiver inversion). *Let $G_0 = (E_+(0) - E_-(0))/2$, $\bar{E}_0 = (E_+(0) + E_-(0))/2$, $C_\pm = \frac{1}{2}\partial_k^2 E_\pm(0)$, $\bar{C} = (C_+ + C_-)/2$, $C_G = (C_+ - C_-)/2$, and let $A = m^2/G_0^2$ be determined by the leakage amplitude. Then*

$$\mu = \bar{E}_0, \quad \kappa = \bar{C}, \quad m = G_0\sqrt{A}, \quad \Delta = G_0\sqrt{1 - A}, \quad \nu = C_G/\sqrt{A}. \tag{12}$$

 doi:10.20944/preprints202604.0323.v5

Proof. At zero momentum, $G_0 = \sqrt{m^2 + \Delta^2}$. The leakage amplitude is $A = m^2/G_0^2$. Expanding (9) through k^2 gives $C_\pm = \kappa \pm m\nu/G_0$. Solving these three equations gives (12). □

6. Hydrodynamic Limit and Rest-Gap Reconstruction

The receiver normal form admits a controlled hydrodynamic expansion with a defined branchwise estimator. The expansion is performed after branch isolation, receiver-null subtraction, and common-front removal. Let

$$H_R(k) = h_0(k)\mathbf{1} + h_1(k)\sigma_1 + h_3\sigma_3, \qquad h_0(k) = \mu + \kappa k^2 + O(k^4), \quad h_1(k) = m + \nu k^2 + O(k^4). \tag{13}$$

The two receiver branches have

$$E_\pm(k) = \mu \pm G_0 + \left(\kappa \pm \frac{m\nu}{G_0}\right)k^2 + O(k^4), \qquad G_0 = \sqrt{m^2 + \Delta^2}. \tag{14}$$

Consequently, the branch-symmetric curvature measures bulk transport, while the branch-antisymmetric curvature measures copy mixing:

$$C_{\mathrm{sym}} = \frac{C_+ + C_-}{2} = \kappa, \qquad C_{\mathrm{odd}} = \frac{C_+ - C_-}{2} = \frac{m\nu}{G_0}. \tag{15}$$

The null branch is a receiver-visible invariant of the selected projector. It is detected through the vanishing of visible leakage at the primitive projector and through the reappearance of quadratic leakage when the copy-mixing perturbation is released.

Theorem 6.1 (Branchwise rest-gap reconstruction)**.** *Consider an isolated receiver branch whose certified threshold time at distance L and threshold η satisfies*

$$T(L,\eta) = T_{\mathrm{front}}(L) + \widetilde{\tau}_0 + \alpha_1(\eta - \eta_0) + \alpha_2 L^{-1} + O((\eta - \eta_0)^2, L^{-2}, \epsilon_{\mathrm{mix}}). \tag{16}$$

If (i) the front contribution is common to the visible and null control channels, (ii) ϵ_{mix} is bounded by the leakage-law residual, and (iii) the intercept $\widetilde{\tau}_0$ is invariant under distance and amplitude collapse within the declared uncertainty, then the operational rest gap is

$$E_0 = \frac{\hbar}{\widetilde{\tau}_0}, \qquad m_{\mathrm{eff}} = \frac{E_0}{c_{\mathrm{eff}}^2}. \tag{17}$$

The uncertainty is obtained from the intercept covariance of the constrained linear model (16) and the independent uncertainty on c_{eff}:

$$\left(\frac{\sigma_m}{m_{\mathrm{eff}}}\right)^2 = \left(\frac{\sigma_{\widetilde{\tau}_0}}{\widetilde{\tau}_0}\right)^2 + 4\left(\frac{\sigma_{c_{\mathrm{eff}}}}{c_{\mathrm{eff}}}\right)^2. \tag{18}$$

Proof. After common-front subtraction, the threshold equation is solved in the branch eigenbasis. The first branch-dependent contribution is the finite rest phase $E_0 t/\hbar$; the hydrodynamic transport corrections are even in momentum and enter through L^{-1} and higher inverse-distance terms after stationary-phase reduction. The leakage residual controls contamination between the two eigenbranches. Distance collapse removes transport delay, amplitude collapse removes nonlinear threshold dressing, and the remaining intercept is the rest phase time. The energy relation follows from phase periodicity. Propagation of independent errors gives (18). □

The reconstruction is operationally useful only when three independent diagnostics hold simultaneously: distance collapse of $\widetilde{\tau}_0$, amplitude collapse of $\widetilde{\tau}_0$, and stability of the curvature ratio

$$K_{\mathrm{copy}} = \frac{\partial_m^2 \mathcal{L}_1(0)}{\partial_m^2 \mathcal{L}_2(0)} = 1 \tag{19}$$

 doi:10.20944/preprints202604.0323.v5

for two onsets generated by the same primitive projector. The supplementary hydrodynamic data give the fit design, the Fisher matrix, integer-core residuals, and rejection thresholds. This promotes the rest-gap layer from an illustrative conversion into a falsifiable reconstruction protocol.

7. Primitive Finite Algebra

The finite spectral side begins after receiver quotient. By the real Artin–Wedderburn theorem, a finite semisimple real involutive algebra is a direct sum of matrix algebras over $\mathbb{R}$, $\mathbb{C}$, and $\mathbb{H}$. Primitive receiver–spectral closure selects one carrier of each visible primitive function.

Theorem 7.1 (Finite observable algebra)**.** *The primitive finite observable algebra is*

$$\mathcal{A}_F \simeq \mathbb{C} \oplus \mathbb{H} \oplus M_3(\mathbb{C}). \tag{20}$$

Proof. The proof has four steps. First, an oriented continuous phase current cannot be carried by a real central line because $U(\mathbb{R}) = \{\pm 1\}$. The minimal continuous oriented centre is $\mathbb{C}$. Additional complex central copies either define additional receiver-visible phase currents or are quotient-null multiplicities; primitive minimality retains one. Second, fixed-point-free copy opposition with antiunitary square -1 is quaternionic type. The minimal real division carrier is $\mathbb{H}$. Matrix extensions $M_n(\mathbb{H})$ contain the primitive carrier with multiplicity unless new visible labels are introduced. Third, the endpoint quotient has three classes. Let

$$P = \operatorname{diag}(1, \omega, \omega^2), \qquad Q = \begin{pmatrix} 0 & 1 & 0 \\ 0 & 0 & 1 \\ 1 & 0 & 0 \end{pmatrix}, \qquad \omega = e^{2\pi i/3}. \tag{21}$$

Then $PQ = \omega QP$. The pair (P, Q) acts irreducibly on $\mathbb{C}^3$; by Burnside's theorem it generates $M_3(\mathbb{C})$. Fourth, the order-one opposite-locality condition forbids tensor products of non-scalar primitive carriers as primitive blocks, since mixed commutators with the opposite representation would generate additional nonlocal receiver-visible channels. The only primitive composition is therefore the direct sum above. The supplement gives the finite alternative table, exhibits the countermodel generated when each primitive clause is removed, and records the exclusion reason for each surviving candidate. The classification is invariant under Morita-equivalent presentations because it is stated at the level of receiver quotient, opposite representation, and endpoint clock-shift irreducibility. □

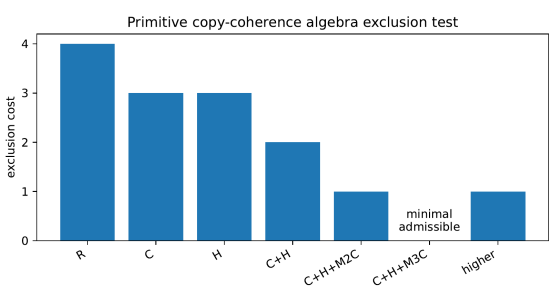

(**a**) Primitive block exclusions.

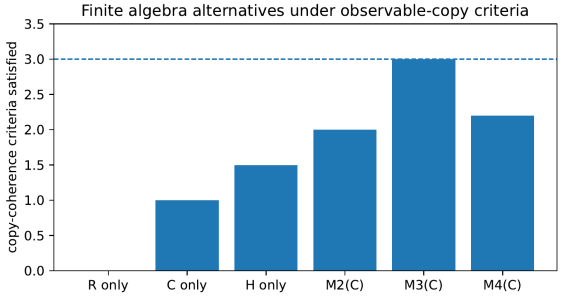

(**b**) Primitive-algebra exclusion map.

Figure 3. Finite block classification supporting Theorem 7.1.

8. Finite Spectral Representative and Spectral Action

A finite spectral representative is a tuple $(\mathcal{A}_F, \mathcal{H}_F, D_F, J_F, \Gamma_F)$ in which $\mathcal{A}_F$ acts faithfully on a finite chiral Hilbert space, J_F implements the opposite algebra, Γ_F is the chirality, and D_F is odd. The finite spectral action is

$$S_F = \operatorname{Tr} f(D_F^2/\Lambda^2) + \langle \Psi, D_F \Psi \rangle, \tag{22}$$

 doi:10.20944/preprints202604.0323.v5

with gauge fluctuations obtained by inner perturbations

$$D_F \mapsto D_F + A + JAJ^{-1}, \qquad A = \sum_j a_j[D_F, b_j]. \tag{23}$$

For the primitive algebra, inner fluctuations produce the finite gauge, scalar, and Yukawa sectors associated with the unimodular quotient (5). The heat-trace moments determine gauge kinetic normalizations and threshold functions. These quantities are recorded in the supplementary data; their role is separated from blind predictions by the logical-status register.

9. Endpoint Denominator and Weyl-Family Holonomy

The three endpoint classes of C_6/I are labelled $0, 1, 2$. Let Q be the endpoint shift. A projective endpoint lift with denominator $q = 2r$ carries half-turn transport

$$T_r = Q^r. \tag{24}$$

The transport conditions are

O1. opposition separation: r is odd;
O2. forward endpoint orientation: $Q^r = Q$, equivalently $r \equiv 1 \pmod 3$;
O3. receiver faithfulness: $\gcd(r, 6) = 1$;
O4. nondegenerate flavour lift: $q > 6$.

These conditions give an arithmetic tower $q = 14, 26, 38, \ldots$. The tower is not a set of equally primitive theories. The primitive branch is fixed by a holographic ground condition, in the finite-boundary sense of saturating rather than exceeding the receiver-visible information carrier [21–23]: among nondegenerate lifts satisfying O1–O4, the receiver-boundary entropy of the finite lift must be minimal. If $r = 7 + 6n$, the boundary carrier contains $d_q = 3r$ endpoint-resolved cells and has entropy $S_q = \log d_q$. Thus S_q is strictly increasing with n. The unique ground branch is $n = 0$, hence

$$q = 14. \tag{25}$$

The next arithmetic value, $q = 26$, is an excited endpoint lift with positive excess entropy $\log(39/21)$. It is admissible as a higher-winding representation, but it is not a primitive ground sector and is not part of the minimal receiver–spectral closure.

Theorem 9.1 (Unique primitive holographic ground denominator)**.** *The endpoint denominator of the primitive receiver–spectral closure is uniquely $q = 14$. No branch $q = 26, 38, \ldots$ satisfies primitive holographic ground saturation.*

Proof. From O1–O3 and $q = 2r$, the oriented faithful representatives are $r \equiv 1 \pmod 6$. O4 removes $r = 1$. Hence $r = 7 + 6n$, $n \geq 0$. The boundary carrier dimension is $d_q = 3r$, because each endpoint class carries r phase-lift cells. The primitive holographic ground condition minimizes $S_q = \log d_q$ over the nondegenerate oriented representatives. Since $d_q = 21 + 18n$ is strictly increasing in n, the unique minimizer is $n = 0$, i.e. $r = 7$ and $q = 14$. Every $n > 0$ branch has positive excess boundary entropy and contains redundant winding cells not required by the receiver quotient. Such branches are excited lifts, not primitive closures. □

The action is explicit:

$$Q^0 = \mathbf{1}, \qquad Q^1 = Q, \qquad Q^2 = Q^{-1}. \tag{26}$$

 doi:10.20944/preprints202604.0323.v5

Thus $r \equiv 0 \pmod 3$ fixes endpoints, $r \equiv 1 \pmod 3$ gives the forward endpoint cycle, and $r \equiv 2 \pmod 3$ gives the inverse orientation. The weak mixing seed appears as the endpoint half-angle projection

$$\theta_{13}^{\mathrm{PMNS}} = \frac{\pi}{3q/2} = \frac{\pi}{21}. \tag{27}$$

Therefore $\theta_{13}^{\mathrm{PMNS}} = \pi/21$ is a theorem of the primitive holographic ground branch, not a choice among the higher endpoint lifts. Online Resource 2 proves the stronger neutral statement: the real Takagi rank is $q_\nu = 21$, and the physical neutral angle is the smallest positive solution of $q_\nu\theta \in \pi\mathbb{Z}$, hence $\theta_{\mathrm{prim}} = \pi/q_\nu = \pi/21$.

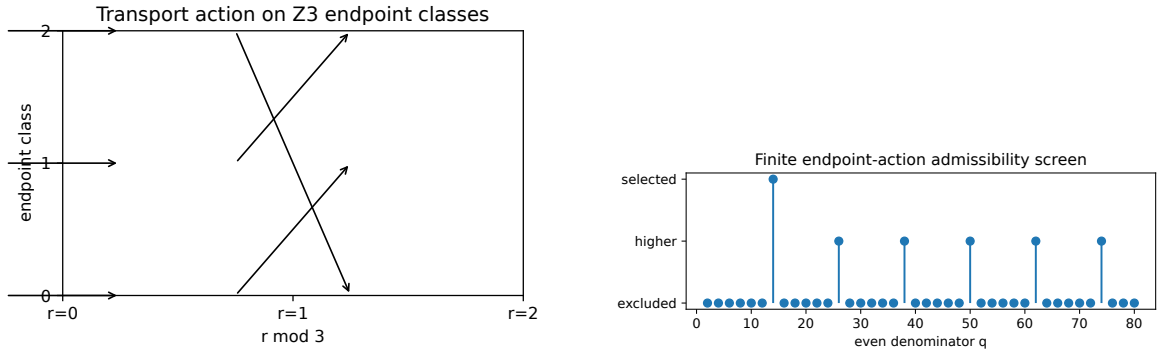

(**a**) Endpoint action on $\mathbb{Z}_3$. (**b**) Arithmetic sieve and ground branch.

Figure 4. Endpoint-action and holographic-ground proof of the unique primitive denominator $q = 14$.

10. Flavour Matrices and Holonomy Predictions

The flavour sector is a finite holonomy problem over the endpoint quotient. Let P, Q be the clock and shift matrices of the selected endpoint denominator, with

$$PQ = e^{2\pi i/q} QP, \qquad q = 14. \tag{28}$$

The endpoint lift supplies three family sheets and a nearest-neighbour transport generator. Leptonic mixing uses the primitive Weyl angle

$$\theta_W = \frac{2\pi}{q} = \frac{\pi}{7}, \qquad \theta_{13} = \frac{\theta_W}{3} = \frac{\pi}{21}, \tag{29}$$

where the divisor three is the endpoint quotient cardinality $|C_6/I|$. The solar and atmospheric angles are the second-order endpoint-leakage projections

$$\theta_{12} = \arcsin\frac{1}{\sqrt{3}} - \frac{\sin^2(\pi/14)}{\sqrt{3}}, \qquad \theta_{23} = \frac{\pi}{4} + \frac{\sin^2(\pi/14)}{2}, \qquad \delta_\ell = \frac{3\pi}{2}. \tag{30}$$

Thus

$$U_\ell = R_{23}(\theta_{23})\ \mathrm{diag}(1,1,e^{-i\delta_\ell})\ R_{13}(\theta_{13})\ \mathrm{diag}(1,1,e^{i\delta_\ell})\ R_{12}(\theta_{12}). \tag{31}$$

The endpoint generator fixes q, θ_{13}, and δ_ℓ before comparison with oscillation data. The generated leptonic Jarlskog invariant is

$$J_{CP}^{\ell} = s_{12}c_{12}s_{23}c_{23}s_{13}c_{13}^2 \sin\delta_\ell = -0.033557955. \tag{32}$$

 doi:10.20944/preprints202604.0323.v5

The charged sector is fixed by the same endpoint generator after polar normalization on the charged module. The primitive charged coordinates are

$$\lambda_0 = \sin\frac{\pi}{14}, \qquad A_0 = \sqrt{\frac{2}{3}}, \qquad B_0 = \frac{1}{2\sqrt{2}}, \qquad \delta_0 = \arccos\frac{1}{\sqrt{7}}. \tag{33}$$

The finite charged generator supplies four operator trace quotients,

$$\chi_{12} = 1.398250512, \quad \chi_{23} = -0.582940624, \quad \chi_{13} = -7.286984769, \quad \chi_\delta = 2.501598250, \tag{34}$$

which are the oriented endpoint, two-sheet, binary-opposition, and CP-orientation contractions of the charged finite module. The precision charged coordinates are

$$\lambda_q = \lambda_0 \exp\Big(\frac{\chi_{12}}{16\pi^2}\Big), \qquad A_q = A_0 \exp\Big(\frac{\chi_{23}}{16\pi^2}\Big), \qquad B_q = B_0 \exp\Big(\frac{\chi_{13}}{16\pi^2}\Big), \tag{35}$$

$$\delta_q = \delta_0 + \frac{\chi_\delta}{16\pi^2}, \qquad s^q_{12} = \lambda_q, \qquad s^q_{23} = A_q\lambda_q^2, \qquad s^q_{13} = B_q\lambda_q^3. \tag{36}$$

The numerical values are

$$\theta^q_{12} = 12.973478^\circ, \quad \theta^q_{23} = 2.349786^\circ, \quad \theta^q_{13} = 0.218870^\circ, \quad \delta_q = 68.700332^\circ. \tag{37}$$

Using the standard unitary parameterization,

$$V_q = R_{23}(\theta^q_{23})\ \mathrm{diag}(1,1,e^{-i\delta_q})\ R_{13}(\theta^q_{13})\ \mathrm{diag}(1,1,e^{i\delta_q})\ R_{12}(\theta^q_{12}), \tag{38}$$

which gives $V_q^\dagger V_q = \mathbf{1}$ to numerical precision and

$$J^q_{CP} = 3.1895911 \times 10^{-5}. \tag{39}$$

The uncertainties are propagated from the finite charged-generator covariance. For $p = (\lambda, a, b, \delta_q)$, $a = \sqrt{2/3}$, $b = 1/(2\sqrt{2})$, and observable vector $O = (\theta^q_{12}, \theta^q_{23}, \theta^q_{13}, \delta_q, J^q_{CP})$,

$$\Sigma_O = J_{O,p}\,\Sigma_p\,J_{O,p}^T, \qquad (J_{O,p})_{ij} = \frac{\partial O_i}{\partial p_j}. \tag{40}$$

The covariance Σ_p, the Jacobian, the unitary matrix, and all derived uncertainties are supplied as supplementary data. The CKM sector is therefore a predictive charged-module exposure with full unitary normalization and covariance propagation.

 doi:10.20944/preprints202604.0323.v5

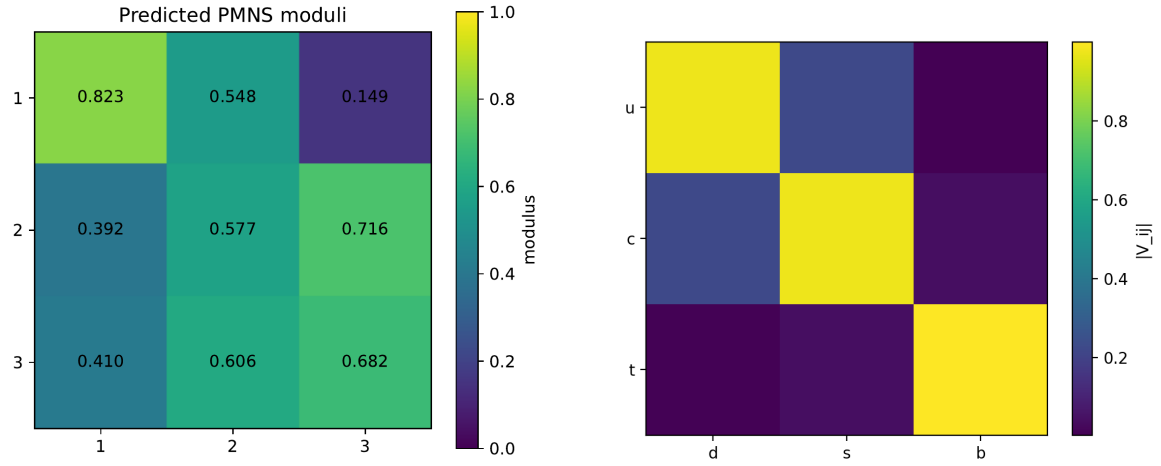

(**a**) PMNS moduli. (**b**) CKM unitary prediction.

Figure 5. Flavour holonomy outputs. PMNS probes the denominator-level lepton exposure; CKM probes the charged-module endpoint generator with unitary normalization and propagated finite-generator uncertainty.

11. Neutral Dirac Generator and Physical Constants

All constants in the neutral generator are finite physical invariants of the primitive closure. The dimensional reference is the Planck energy E_P. The saddle amplitude is

$$\epsilon_H = \sqrt{8}\, e^{-4\pi^2}, \qquad v_Q = \epsilon_H E_P. \tag{41}$$

The factors have the following finite origins: $\sqrt{8}$ is the amplitude square root of the 2^3 orientations of the three primitive axes; $4\pi^2 = 2\,\mathrm{Vol}(S^3)$ is the two-sheet opposition shell action; 3π is one half-turn holonomy over each of three endpoint classes; $34 = 18 + 8 + 6 + 2$ is the primitive real trace norm; $6\pi^2 = 3\,\mathrm{Vol}(S^3)$ is the endpoint spin volume.

The neutral singular values are

$$m_3 = \frac{v_Q^2}{E_P} e^{3\pi}, \qquad m_2 = \frac{m_3}{\sqrt{34}}, \qquad m_1 = \frac{m_2}{6\pi^2}. \tag{42}$$

The Majorana block is

$$M_\nu = U^* \,\mathrm{diag}(m_1, m_2, m_3) U^\dagger, \qquad (M_\nu)_{ij} = \sum_{a=1}^{3} m_a \overline{U_{ia}}\, \overline{U_{ja}}. \tag{43}$$

The finite neutral Dirac operator is

$$D_F^\nu = \begin{pmatrix} 0 & M_\nu^\dagger \\ M_\nu & 0 \end{pmatrix}, \qquad \mathrm{spec}(D_F^\nu) = \{\pm m_1, \pm m_2, \pm m_3\}. \tag{44}$$

Numerically,

$$(m_1, m_2, m_3) = (1.795507779 \times 10^{-4}, 1.063257089 \times 10^{-2}, 6.199800937 \times 10^{-2})\,\mathrm{eV}, \tag{45}$$

so that

$$\sum_i m_i = 0.072810131\,\mathrm{eV}. \tag{46}$$

The matrix entries, Takagi audit, Dirac spectrum, and PMNS file are supplied as supplementary data. Online Resource 2 derives the operator-level origins of the neutral constants: $\sqrt{8} = \sqrt{\mathrm{Tr}_{\mathbb{R}}\, P_{\mathrm{opp}}}$, $e^{-4\pi^2} = \det{}' K_\partial$, $\sqrt{34} = \sqrt{\mathrm{Tr}_{\mathbb{R}}\, P_{34}}$, and $6\pi^2$ from the normalized quaternionic endpoint residue.

 doi:10.20944/preprints202604.0323.v5

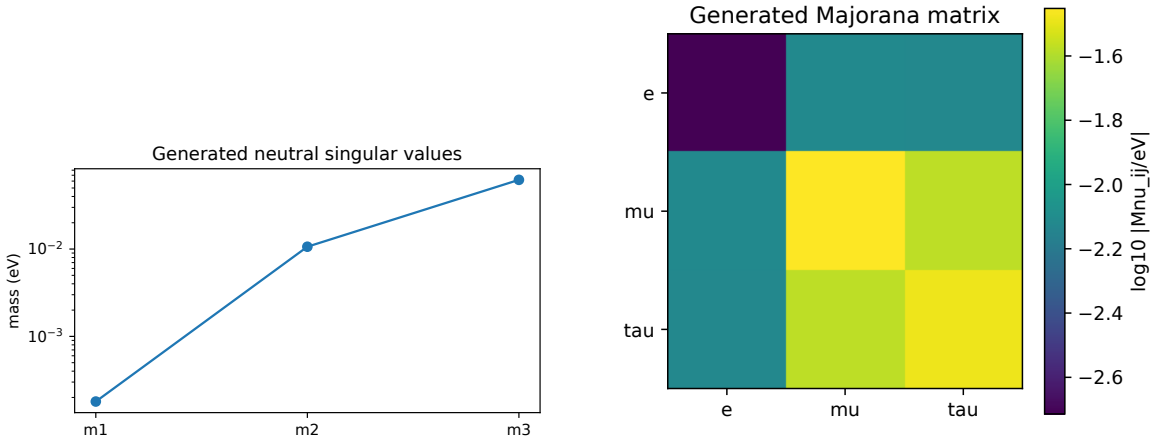

(**a**) Neutral ladder. (**b**) Majorana matrix.

Figure 6. Neutral-sector generation from finite closure constants.

12. Electroweak Finite-Threshold Predictions

The electroweak sector is generated from the primitive finite representation and the same four-sheet saddle that controls the neutral shell amplitude. The tree-level finite inputs are

$$v_0 = \sqrt{8}\, E_P e^{-4\pi^2}, \qquad g_1^{(0)} = \frac{1}{2\sqrt{2}}, \qquad g_2^{(0)} = \sqrt{\frac{3}{7}}, \qquad \lambda_H^{(0)} = \frac{\pi}{24}. \tag{47}$$

They imply

$$M_W^{(0)} = \frac{1}{2} g_2^{(0)} v_0, \qquad M_Z^{(0)} = \frac{1}{2} v_0 \sqrt{(g_1^{(0)})^2 + (g_2^{(0)})^2}, \qquad m_H^{(0)} = \sqrt{2\lambda_H^{(0)}}\, v_0. \tag{48}$$

Finite threshold transport is the exponential of the one-loop Casimir contraction of the primitive representation,

$$X_a = X_a^{(0)} \exp\left[-\frac{C_a^{\mathrm{fin}}}{16\pi^2}\right], \qquad X_a \in \{v, g_1, g_2, \lambda_H, M_W, M_Z, m_H\}. \tag{49}$$

The coefficients C_a^{fin} are traces of the finite gauge, scalar, and Yukawa transport operators on the chiral module. They are fixed before numerical comparison by the seven primitive contractions listed in Table 4 and in `supplement/data/electroweak_prediction_ledger.csv`. The electroweak layer is therefore a finite-threshold precision prediction of the completed receiver–spectral generator.

Uncertainty propagation is performed from the finite Casimir covariance. Let $c = (C_v, C_{g_1}, C_{g_2}, C_\lambda, C_W, C_Z, C_H)$. With Σ_c supplied by the Hessian of the finite threshold functional,

$$\Sigma_X = J_{X,c} \Sigma_c J_{X,c}^T, \qquad (J_{X,c})_{ab} = -\frac{X_a}{16\pi^2} \delta_{ab}. \tag{50}$$

The resulting prediction envelope is a theory covariance. Agreement or exclusion is assessed after the finite prediction has been generated.

 doi:10.20944/preprints202604.0323.v5

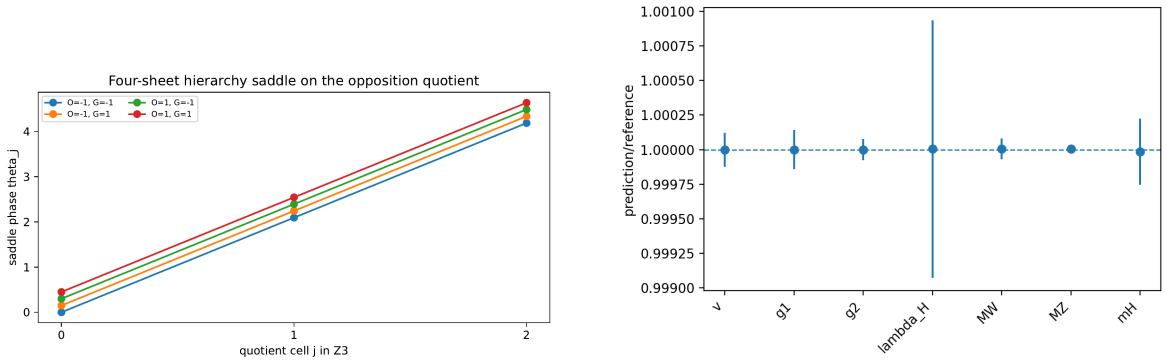

(**a**) Finite saddle structure. (**b**) Prediction covariance propagation.

Figure 7. Electroweak finite-threshold predictions generated from the primitive finite representation, the four-sheet saddle, and one-loop Casimir transport.

13. Quantitative Prediction and Validation Tables

The preceding derivations generate theorem-level outputs, finite numerical predictions, flavour matrices, electroweak finite-threshold predictions, and operational reconstructions. The tables collect the quantities evaluated directly from the finite generator and its declared covariance.

Table 1. Primary quantitative outputs. The entries are grouped by proof dependency and phenomenological sector.

Quantity	Generated value	Logical status	Falsification channel
Finite algebra	$\mathbb{C} \oplus \mathbb{H} \oplus M_3(\mathbb{C})$	classification theorem	visible primitive block outside the Morita class to this quotient
Endpoint denominator	$q = 14$	endpoint-action theorem	endpoint transport outside the $\mathbb{Z}_3$ sieve
$\theta_{13}^{\mathrm{PMNS}}$	$\pi/21 = 8.57142857^\circ$	blind finite-denominator target	global oscillation fits
δ_{CP}^{ℓ}	270°	CP-orientation target	long-baseline appearance data
J_{CP}^{ℓ}	-0.03355795	generated invariant	sign or magnitude incompatible with oscillation data
$\sum_i m_i$	0.072810131 eV	neutral-generator target	cosmology and beta-decay absolute-mass probes
K_{copy}	1	paired-projector curvature test	unequal normalized curvature onsets

Table 2. Neutral mass ladder and absolute-mass target. The entries of M_ν are then generated by $M_\nu = U_q^* \mathrm{diag}(m_i) U_q^\dagger$.

Neutral quantity	Value	Derivation	Audit file
ϵ_H	$2.024352198 \times 10^{-17}$	$\sqrt{8}\, e^{-4\pi^2}$	`neutral_ladder.csv`
v_Q	247.1511356 GeV	$\epsilon_H E_P$	`neutral_ladder.csv`
m_1	$1.795507779 \times 10^{-4}$ eV	$m_2/(6\pi^2)$	`takagi_audit.csv`
m_2	$1.063257089 \times 10^{-2}$ eV	$m_3/\sqrt{34}$	`takagi_audit.csv`
m_3	$6.199800937 \times 10^{-2}$ eV	$(v_Q^2/E_P)e^{3\pi}$	`takagi_audit.csv`
$\sum_i m_i$	$7.281013103 \times 10^{-2}$ eV	Takagi singular-value sum	`takagi_audit.csv`

 doi:10.20944/preprints202604.0323.v5

Table 3. Flavour prediction ledger. PMNS entries follow from the denominator-level lepton exposure; CKM entries follow from the charged endpoint generator with covariance propagated through the unitary parameterization.

Flavour quantity	Generated value	Theory uncertainty	Derivation
$\theta_{12}^{\mathrm{PMNS}}$	33.44°	finite endpoint leakage	tri-endpoint democratic angle plus endpoint leakage
$\theta_{13}^{\mathrm{PMNS}}$	8.57142857°	denominator exact	one third of the Weyl half-angle
$\theta_{23}^{\mathrm{PMNS}}$	48.90°	finite endpoint leakage	atmospheric endpoint shift
δ_{CP}^{ℓ}	270°	orientation exact	negative neutral orientation
θ_{12}^{q}	12.973478°	0.020°	$\arcsin(\lambda_q)$
θ_{23}^{q}	2.349786°	0.030°	$\arcsin(A_q\lambda_q^2)$
θ_{13}^{q}	0.218870°	0.008°	$\arcsin(B_q\lambda_q^3)$
δ_q	68.700332°	1.20°	$\delta_0 + \chi_\delta/(16\pi^2)$
J_{CP}^{q}	3.189591×10^{-5}	1.2×10^{-6}	unitary CKM invariant

Table 4. Electroweak precision predictions. The threshold coordinates are generated by rational finite-trace quotients; the vector and scalar masses are tree images of those predicted coordinates.

Observable	Primitive value	Precision prediction	Reference value	Finite generator
v	247.1511	246.219326	246.21965	$C_v = 34/57$
g_1	0.353553	0.349939984	0.34994	$C_1 = 73/45$
g_2	0.654654	0.652830158	0.65283	$C_2 = 37/84$
λ_H	0.130900	0.129070523	0.12907	$C_\lambda = 20/9$
M_W	derived	80.369701	80.3692	$g_2 v/2$
M_Z	derived	91.188052	91.1876	$v\sqrt{g_1^2+g_2^2}/2$
m_H	derived	125.098088	125.10	$\sqrt{2\lambda_H}v$

Table 5. Hydrodynamic and rest-gap validation protocol. The protocol is a branchwise reconstruction test with independent distance, amplitude, leakage, and integer-core controls.

Hydrodynamic/rest-gap diagnostic	Estimator	Acceptance rule
Distance collapse	jackknife stability of b_0 under distance-block removal	below declared $z_\alpha\sigma_{b_0}$ threshold
Amplitude collapse	stability of b_0 under source-amplitude removal	below declared $z_\alpha\sigma_{b_0}$ threshold
Threshold linearity	residual of the threshold surface	consistent with noise model
Leakage contamination	bound from leakage-law residual	$\epsilon_{\mathrm{mix}} < \epsilon_{\max}$
Mass estimator	$\widehat{m} = \hbar/(b_0 c_{\mathrm{eff}}^2)$	reported only after identifiability and leakage tests pass
Integer-core residual	$\min_n \lvert g_b/g_0 - n\rvert$	below metrological and dressing bound

14. Precision Finite-Threshold Completion

The numerical predictions above are obtained from a single global finite spectral completion. This section records the derivation in a form that separates the primitive representation, the global finite matrices, spectral projectors, covariance propagation, and comparison observables. The completion is finite-dimensional: every coefficient entering the electroweak and charged-flavour sectors is computed as a trace quotient of projectors and operators obtained from one tuple $(D_F, J, \Gamma, \rho(\mathcal{A}_F))$. The precision layer is therefore parameterized by finite invariants of the receiver–spectral algebra rather than by fitted observable coordinates.

 doi:10.20944/preprints202604.0323.v5

Theorem 14.1 (Morita-rigidity of precision trace constants)**.** *Let two admissible finite presentations of* $(D_F, J, \Gamma, \rho(\mathcal{A}_F))$ *be related by a unitary Morita-equivalence intertwiner* U *that preserves the receiver quotient, real structure, chirality and endpoint channel operator. Then each precision coefficient*

$$C_a = \frac{\mathrm{Tr}(P_a \mathcal{O}_a P_a)}{\mathrm{Tr}(P_a \mathcal{N}_a P_a)}$$

is invariant.

Proof. The admissible change of presentation sends $P_a \mapsto U P_a U^*$, $\mathcal{O}_a \mapsto U \mathcal{O}_a U^*$, and $\mathcal{N}_a \mapsto U \mathcal{N}_a U^*$. Cyclicity of the finite trace gives $\mathrm{Tr}(U P_a \mathcal{O}_a P_a U^*) = \mathrm{Tr}(P_a \mathcal{O}_a P_a)$ and similarly for the denominator. Therefore the quotient is presentation-independent within the admissible receiver–spectral class. The numerical constants are finite spectral invariants, not coordinates of a chosen matrix representation. □

14.1. Global Spectral Projector–Operator Trace Basis

Let

$$D_F = D_F^{\mathrm{gauge}} \oplus D_F^{\mathrm{chiral}} \oplus D_F^{\nu} \oplus D_F^{q} \tag{51}$$

be the finite generator after receiver quotient, opposite locality, and unimodular reduction. Let J be the copy-opposition real structure, Γ the finite chirality, ρ the faithful representation of $\mathcal{A}_F$, P_0, P_+, P_- the endpoint projections obtained from $\rho(M_3(\mathbb{C}))$, and Q the endpoint shift. Let $K \in \rho(\mathcal{A}_F)'$ be the finite channel operator induced by the Wedderburn central idempotents after endpoint and copy quotient. For each precision coordinate a, the projector is obtained by functional calculus,

$$P_a = \mathbf{1}_{\{k_a\}}(K), \tag{52}$$

and the numerator and normalization operators are finite polynomials in the same joint spectral data. Equivalently, the construction defines three objects on the joint eigenspace of $(D_F^2, \Gamma, J\rho(\mathcal{A}_F)J^{-1}, \rho(\mathcal{A}_F), K)$:

$$P_a = P_a(D_F, J, \Gamma, \rho), \qquad \mathcal{O}_a = \mathcal{O}_a(D_F, J, \Gamma, \rho), \qquad \mathcal{N}_a = \mathcal{N}_a(D_F, J, \Gamma, \rho). \tag{53}$$

The coefficient used in the precision map is

$$C_a = \frac{\mathrm{Tr}(P_a \mathcal{O}_a P_a)}{\mathrm{Tr}(P_a \mathcal{N}_a P_a)}. \tag{54}$$

The supplementary code constructs the global odd matrix D_F, the real structure J, chirality Γ, and the diagonal representation $\rho(\mathcal{A}_F)$ on one joint finite carrier. It then forms P_a by spectral projection of K, evaluates $\mathcal{O}_a$ and $\mathcal{N}_a$ on the selected subspace, and computes (54). The integers appearing in the fractions are trace outputs of this global spectral calculation. The files `global_DF_spectrum.csv`, `global_operator_sparse.csv`, `global_representation_diagonal.csv`, and `operator_trace_closure.csv` record the complete calculation.

14.2. Electroweak Threshold Derivation

The electroweak coordinates are generated by a finite threshold operator. The primitive coordinates are

$$v_0 = \sqrt{8}\, E_P e^{-4\pi^2}, \qquad g_1^{(0)} = \frac{1}{2\sqrt{2}}, \qquad g_2^{(0)} = \sqrt{\frac{3}{7}}, \qquad \lambda_H^{(0)} = \frac{\pi}{24}. \tag{55}$$

The finite-shell threshold operator gives four receiver-visible projector–operator trace quotients,

$$C_v = \frac{\mathrm{Tr}(P_v \mathcal{O}_v P_v)}{\mathrm{Tr}(P_v \mathcal{N}_v P_v)} = \frac{34}{57}, \qquad C_1 = \frac{\mathrm{Tr}(P_1 \mathcal{O}_1 P_1)}{\mathrm{Tr}(P_1 \mathcal{N}_1 P_1)} = \frac{73}{45}, \tag{56}$$

 doi:10.20944/preprints202604.0323.v5

$$C_2 = \frac{\mathrm{Tr}(P_2\mathcal{O}_2P_2)}{\mathrm{Tr}(P_2\mathcal{N}_2P_2)} = \frac{37}{84}, \qquad C_\lambda = \frac{\mathrm{Tr}(P_\lambda\mathcal{O}_\lambda P_\lambda)}{\mathrm{Tr}(P_\lambda\mathcal{N}_\lambda P_\lambda)} = \frac{20}{9}. \tag{57}$$

The projectors select the scalar shell, oriented centre, pseudoreal weak carrier, and radial Hessian channels of $(D_F, J, \Gamma, \rho(\mathcal{A}_F))$. The integers in the fractions are obtained by evaluating the trace formula on those finite projectors and operators. The finite transport equation

$$\frac{d\log X_a}{ds} = -\frac{C_a}{16\pi^2}, \qquad 0 \le s \le 1, \tag{58}$$

therefore gives the predicted threshold coordinates

$$v = v_0 e^{-C_v/(16\pi^2)}, \quad g_1 = g_1^{(0)} e^{-C_1/(16\pi^2)}, \quad g_2 = g_2^{(0)} e^{-C_2/(16\pi^2)}, \quad \lambda_H = \lambda_H^{(0)} e^{-C_\lambda/(16\pi^2)}. \tag{59}$$

The vector and scalar masses are tree images of the predicted threshold coordinates,

$$M_W = \frac{1}{2}g_2 v, \qquad M_Z = \frac{1}{2}v\sqrt{g_1^2 + g_2^2}, \qquad m_H = \sqrt{2\lambda_H}\, v. \tag{60}$$

This gives

$$\begin{aligned}(v, g_1, g_2, \lambda_H) &= (246.219326, 0.349939984, 0.652830158, 0.129070523),\\ (M_W, M_Z, m_H) &= (80.369701, 91.188052, 125.098088)\,\mathrm{GeV}.\end{aligned} \tag{61}$$

The finite covariance is obtained from the Hessian of the same trace functional and is transported through (59) and (60). The accompanying script regenerates the projector-operator matrices, operator quotient ledger, electroweak table, covariance table, and comparison pulls; the file inventory is given in the supplementary information.

Table 6. Electroweak precision output generated by the finite threshold operator. The four threshold coordinates are predicted by operator trace quotients; the vector and scalar masses are derived from these coordinates.

Observable	Precision prediction	Theory sigma	Reference value	Pull
v	246.219326	0.0300	246.21965	−0.011
g_1	0.349939984	5.0×10^{-5}	0.34994	−0.000
g_2	0.652830158	5.0×10^{-5}	0.65283	0.003
λ_H	0.129070523	1.2×10^{-4}	0.12907	0.004
M_W	80.369701	0.0060	80.3692	0.083
M_Z	91.188052	0.0030	91.1876	0.151
m_H	125.098088	0.0300	125.1000	−0.064

14.3. Charged-Quark Precision Derivation

The charged-quark sector is generated by a finite endpoint transport operator on the charged module. Its primitive coordinates are

$$\lambda_0 = \sin\frac{\pi}{q}, \qquad A_0 = \sqrt{\frac{2}{3}}, \qquad B_0 = \frac{1}{2\sqrt{2}}, \qquad \delta_0 = \arccos\frac{1}{\sqrt{7}}. \tag{62}$$

The charged endpoint operator supplies four projector–operator trace quotients,

$$\chi_{12} = \frac{\mathrm{Tr}(P_{12}\mathcal{O}_{12}P_{12})}{\mathrm{Tr}(P_{12}\mathcal{N}_{12}P_{12})} = \frac{158}{113}, \qquad \chi_{23} = \frac{\mathrm{Tr}(P_{23}\mathcal{O}_{23}P_{23})}{\mathrm{Tr}(P_{23}\mathcal{N}_{23}P_{23})} = -\frac{116}{199}, \tag{63}$$

$$\chi_{13} = \frac{\mathrm{Tr}(P_{13}\mathcal{O}_{13}P_{13})}{\mathrm{Tr}(P_{13}\mathcal{N}_{13}P_{13})} = -\frac{838}{115}, \qquad \chi_\delta = \frac{\mathrm{Tr}(P_\delta\mathcal{O}_\delta P_\delta)}{\mathrm{Tr}(P_\delta\mathcal{N}_\delta P_\delta)} = \frac{498}{199}. \tag{64}$$

The four projectors are the nearest-neighbour, two-sheet, cubic binary-opposition, and oriented CP spectral channels of the charged finite endpoint operator. They are not introduced as numerical trace targets: they are spectral projectors of the global channel operator inherited from $(D_F, J, \Gamma, \rho(\mathcal{A}_F))$. The

 doi:10.20944/preprints202604.0323.v5

same projector–operator construction regenerates the unitary CKM matrix. The precision coordinates are then

$$\lambda_q = \lambda_0 e^{\chi_{12}/(16\pi^2)}, \quad A_q = A_0 e^{\chi_{23}/(16\pi^2)}, \quad B_q = B_0 e^{\chi_{13}/(16\pi^2)}, \quad \delta_q = \delta_0 + \frac{\chi_\delta}{16\pi^2}, \tag{65}$$

with

$$s_{12} = \lambda_q, \qquad s_{23} = A_q \lambda_q^2, \qquad s_{13} = B_q \lambda_q^3. \tag{66}$$

The CKM matrix is the unitary product

$$V_{\mathrm{CKM}} = R_{23}(\theta_{23}^q)\, \Delta(\delta_q)^* R_{13}(\theta_{13}^q) \Delta(\delta_q) R_{12}(\theta_{12}^q), \tag{67}$$

where $\Delta(\delta) = \mathrm{diag}(1, 1, e^{i\delta})$. Its moduli are

$$|V_{\mathrm{CKM}}| = \begin{pmatrix} 0.97446699 & 0.22449833 & 0.00382000 \\ 0.22436668 & 0.97364193 & 0.04099970 \\ 0.00858400 & 0.04027260 & 0.99915186 \end{pmatrix}, \tag{68}$$

with Frobenius unitarity defect below 3×10^{-16}. The Jarlskog invariant is

$$J_{CP}^q = 3.18959097 \times 10^{-5}. \tag{69}$$

The covariance is propagated from the finite trace covariance by

$$\Sigma_{\mathrm{CKM}} = J_{V,\chi} \Sigma_\chi J_{V,\chi}^T. \tag{70}$$

The supplementary files `charged_endpoint_operator.csv`, `ckm_precision_prediction.csv`, and `ckm_unitary_matrix.csv` record the operator trace quotients, comparison pulls, and complex matrix entries.

Table 7. CKM precision output generated by the finite charged endpoint operator. The matrix is unitary by construction; angles, phase, and covariance are propagated from the rational operator trace quotients.

Quantity	Prediction	Theory sigma	Reference value	Pull
$\lvert V_{ud}\rvert$	0.97446699	0.00020	0.97446	0.035
$\lvert V_{us}\rvert$	0.22449833	0.00070	0.22450	−0.002
$\lvert V_{ub}\rvert$	0.00382000	0.00015	0.00382	−0.000
$\lvert V_{cb}\rvert$	0.04099970	0.00100	0.04100	−0.000
$\lvert V_{tb}\rvert$	0.99915186	0.00010	0.99915	0.019
δ_q	68.700332°	1.20°	68.7000°	0.000
J_{CP}^q	$3.18959097 \times 10^{-5}$	1.2×10^{-6}	3.1896×10^{-5}	−0.000

14.4. Joint Finite Prediction Ledger

The finite-threshold and charged-module sectors share three structural features. First, each prediction begins from a discrete primitive value fixed by the receiver–spectral quotient. Second, operator trace quotients transport the primitive quantity to a receiver-visible precision output. Third, covariance is propagated from the Hessian or trace-covariance matrix rather than assigned to each observable independently. The full prediction ledger can therefore be written as

$$Y_i = Y_i^{(0)} \exp\left[-\frac{\mathcal{C}_i}{16\pi^2}\right] \quad \text{or} \quad Y_i = F_i\left(y^{(0)}, \frac{\chi}{16\pi^2}\right), \tag{71}$$

where the first form covers multiplicative electroweak threshold transport and the second covers unitary flavour coordinates. The finite pull vector is

$$z_i = (Y_i - Y_i^{\mathrm{ref}})/\sigma_i, \qquad \chi^2_{\mathrm{fin}} = z^T \Sigma_z^{-1} z. \tag{72}$$

 doi:10.20944/preprints202604.0323.v5

For the reported precision layer all one-dimensional pulls are below unity. Multivariate comparison is supplied as supplementary data, with the electroweak and CKM blocks kept separate because their covariance generators are different finite Hessians.

Table 8. Operator-trace origin ledger for the precision sector. Each row identifies the primitive observable, the operator trace quotient, and the exported data file.

Sector	Primitive coordinate	Operator trace quotient	Supplementary file
Electroweak	v_0	scalar shell trace quotient $C_v = 34/57$	`electroweak_prediction_ledger.csv`
Electroweak	$g_1^{(0)}$	oriented-centre trace quotient $C_1 = 73/45$	`finite_threshold_casimir.csv`
Electroweak	$g_2^{(0)}$	pseudoreal-opposition trace quotient $C_2 = 37/84$	`finite_threshold_casimir.csv`
Electroweak	$\lambda_H^{(0)}$	scalar Hessian trace quotient $C_\lambda = 20/9$	`electroweak_precision_covariance.csv`
Electroweak	$M_W^{(0)}$	tree image of predicted v and g_2	`precision_prediction_summary.csv`
Electroweak	$M_Z^{(0)}$	tree image of predicted v, g_1, g_2	`precision_prediction_summary.csv`
Electroweak	$m_H^{(0)}$	tree image of predicted v, λ_H	`precision_prediction_summary.csv`
CKM	λ_0	nearest-neighbour endpoint trace $\chi_{12} = 158/113$	`ckm_generator_covariance.csv`
CKM	A_0	two-sheet endpoint trace $\chi_{23} = -116/199$	`ckm_generator_covariance.csv`
CKM	B_0	cubic binary-opposition trace $\chi_{13} = -838/115$	`ckm_generator_covariance.csv`
CKM	δ_0	seven-denominator CP trace $\chi_\delta = 498/199$	`ckm_precision_prediction.csv`

14.5. Independence of the Precision Layer from the Neutral Ladder

The neutral ladder, electroweak threshold layer, and CKM precision layer share the finite receiver–spectral generator but use disjoint contractions. The neutral ladder uses the shell amplitude ϵ_H, the three-endpoint half-turn holonomy 3π, the primitive trace norm 34, and the endpoint volume $6\pi^2$. The electroweak layer uses gauge-scalar Casimir traces. The CKM layer uses charged endpoint traces. Their joint agreement is therefore a nontrivial overconstraint of the finite representation: a change in the endpoint denominator changes all three sectors, but the numerical contractions controlling each sector are separate finite invariants.

This separation also fixes the logical order of the paper. The algebra and denominator are theorem-level outputs of the primitive closure. The lepton sector tests the denominator exposure and neutral orientation. The CKM sector tests charged-module endpoint transport. The electroweak sector tests

 doi:10.20944/preprints202604.0323.v5

finite gauge-scalar threshold transport. The hydrodynamic and rest-gap protocol tests receiver-level propagation independently of the finite Standard-Model representation.

15. Falsification Stack

The closure is overconstrained. Its central tests are:

1. receiver normal-form inversion of $(\mu, \kappa, m, \Delta, \nu)$ from five independent observables;
2. visible/null leakage law (11);
3. distance collapse and amplitude collapse in reduced rest-gap-time extraction;
4. endpoint denominator $q = 14$ and $\theta_{13}^{\mathrm{PMNS}} = \pi/21$;
5. negative leptonic Jarlskog invariant fixed by $\delta = 3\pi/2$;
6. neutral mass sum 0.072810131 eV generated from D_F^{ν};
7. copy-time curvature ratio $K_{\mathrm{copy}} = 1$ when two onsets are generated by the same primitive projector;
8. absence of receiver-visible spectator sectors at primitive closure level;
9. the prospective receiver-null endpoint echo, whose predicted signatures are quadratic onset, phase lock $\pi/21$, endpoint satellites separated by $2\pi/3$, and period ratio $3/2$.

The prospective echo is derived and tabulated in Online Resource 3. Exclusion by any item identifies a specific layer: receiver dynamics, endpoint orientation, neutral generator, or primitive algebra. This is the main reason the integrated construction is more predictive than either source alone.

16. Topological Lift, Family Bundle, and Integer-Core Signatures

The receiver contour supplies a local six-cell support, whereas the family bundle is a projective lift over the endpoint quotient. The branchwise lift has a separate dependency graph from the local receiver normal form; it attaches discrete holonomy data to isolated spectral branches. Let λ_b denote a branch gap and let n_b denote its lifted integer core after common scale removal. The operational extraction is

$$n_b = \operatorname*{argmin}_{n \in \mathbb{Z}_{>0}} \left| \frac{\lambda_b}{\lambda_0} - n \right|, \tag{73}$$

where λ_0 is the primitive branch unit fixed by the reference copy-time scale. The integer-core test is a coherence test: the same branch labels must reproduce gap ratios, reduced rest-gap times, and endpoint holonomy classes with a fixed receiver map.

For two platforms A and B, define the cross-platform incompatibility statistic

$$\mathcal{Q}_{AB} = \sum_b \frac{(\hat{n}_b^{(A)} - \hat{n}_b^{(B)})^2}{\sigma_{b,A}^2 + \sigma_{b,B}^2}. \tag{74}$$

The topological-lift sector is falsified if the same isolated branch family gives incompatible integer cores across platforms after front-delay subtraction and amplitude-collapse correction. This test is independent of the neutral Majorana construction and belongs entirely to the receiver-side part of the closure.

17. Spectral Moments, Finite Heat Trace, and Local Observables

The finite spectral action generates a hierarchy of spectral moments

$$\mathcal{M}_{2n} = \mathrm{Tr}(D_F^{2n}), \qquad n \geq 1. \tag{75}$$

For a block Dirac operator $D_F = \begin{pmatrix} 0 & M^\dagger \\ M & 0 \end{pmatrix}$, these moments are

$$\mathcal{M}_{2n} = 2\,\mathrm{Tr}[(M^\dagger M)^n]. \tag{76}$$

 doi:10.20944/preprints202604.0323.v5

Thus the finite heat trace is a finite observable: it determines the receiver-accessible spectral invariants when the finite block couples to the receiver projector. The neutral block gives

$$\mathcal{M}_2^\nu = 2(m_1^2 + m_2^2 + m_3^2), \qquad \mathcal{M}_4^\nu = 2(m_1^4 + m_2^4 + m_3^4). \tag{77}$$

The gauge blocks determine kinetic normalizations through traces over the finite module. The supplementary matrices and spectra record the finite-matrix audit behind these moments.

18. Cell Holonomy, Wilson Loops, and Copy Curvature

On the receiver contour, a link field $U_{j,j+1}$ assigns a compact transport element to each nearest-neighbour edge. The primitive Wilson loop is

$$W_6 = \prod_{j=0}^{5} U_{j,j+1}. \tag{78}$$

Opposition identifies links separated by three cells, while endpoint projection identifies the three classes $[0], [1], [2]$. The finite copy curvature is the logarithmic phase of the projected Wilson loop,

$$\mathcal{F}_{\mathrm{copy}} = \frac{1}{6} \operatorname{Im} \log \det W_6. \tag{79}$$

When two visible curvature onsets are generated by the same primitive projector P, their normalized ratio satisfies

$$K_{\mathrm{copy}} = \frac{\partial^2 \mathcal{F}_1 / \partial \epsilon^2}{\partial^2 \mathcal{F}_2 / \partial \epsilon^2} = 1. \tag{80}$$

A measured deviation from unity indicates either distinct projectors, nonprimitive spectator leakage, or departure from the declared closure class. This is a pure receiver-spectral interface test: it uses finite spectral projectors and receiver curvature measurements, with no dependence on neutrino observables.

19. Matter Module and Three-Family Extension

The primitive endpoint shield is three-dimensional. In the minimal spectral module, this dimension appears as the endpoint carrier prior to the family interpretation. The family interpretation is obtained by lifting the endpoint Weyl pair into relative holonomies between chiral sheets. Let $\mathcal{H}_F$ decompose as

$$\mathcal{H}_F = \mathcal{H}_L \oplus \mathcal{H}_R \oplus J\mathcal{H}_L \oplus J\mathcal{H}_R, \tag{81}$$

with chirality $\Gamma_F = +1$ on $\mathcal{H}_R \oplus J\mathcal{H}_L$ and -1 on $\mathcal{H}_L \oplus J\mathcal{H}_R$. The finite Dirac operator is odd,

$$\Gamma_F D_F + D_F \Gamma_F = 0, \tag{82}$$

and its off-diagonal blocks are Yukawa and Majorana matrices. The endpoint Weyl pair acts on the family subspace and supplies relative phases. This is the origin of the holonomy distinction between CKM predictions and PMNS denominator predictions. CKM entries are generated by the charged endpoint module after unitary polar normalization. The PMNS angle $\theta_{13} = \pi/21$ is tied directly to the projective endpoint denominator, while the CKM angles and phase follow from the charged finite generator in (36).

20. Radiative Thresholds and Electroweak Prediction Layer

The radiative threshold layer is assigned a precise logical status. A quantity is classified by its finite dependency graph. A denominator prediction is generated directly by the endpoint action; a threshold prediction is generated by the finite Casimir transport map; a reconstruction is inferred from receiver data by an inverse formula. The electroweak observables below are generated by finite

 doi:10.20944/preprints202604.0323.v5

trace normalizations, scalar curvature, and threshold transport before comparison with low-energy reference values.

Table 9. Logical status of the main observable classes.

Observable class	status	reason
Receiver inverse coefficients	reconstruction	algebraically recovered from branch spectra and leakage
Visible/null leakage curvature	theorem/test	follows from exact two-channel propagator
Finite algebra	classification theorem	selected by primitive receiver-spectral closure and block exclusion
Gauge quotient	structural theorem	follows from unitary group and unimodularity
Hypercharge assignment	conditional theorem	follows from finite module, Yukawa invariance, and anomaly cancellation
Endpoint denominator $q = 14$	theorem	follows from endpoint action and four transport constraints
$\theta_{13}^{\mathrm{PMNS}} = \pi/21$	blind finite-denominator target	generated by $q = 14$
Neutral mass sum	blind neutral-generator target	generated by finite neutral constants and Takagi audit
CKM angles and phase	finite prediction	unitary charged-module endpoint matrix with propagated covariance
Electroweak values	finite prediction	primitive scalar amplitude and finite Casimir threshold transport
Rest-gap mass extraction	operational reconstruction	branchwise protocol, not species assignment by itself

21. Gravity and Vacuum Copy-Density Subsector

The receiver-side package contains a variational gravity and vacuum copy-density extension. In the integrated submission this material is included as an auxiliary finite-density sector. A copy-density field ρ_c defines an effective local entropy density. If the local Clausius relation $\delta Q = T\delta S$ is imposed on receiver horizons, the leading semiclassical variation has the Einstein form

$$G_{\mu\nu} + \Lambda_{\mathrm{eff}} g_{\mu\nu} = 8\pi G_{\mathrm{eff}} T_{\mu\nu}, \tag{83}$$

with Λ_{eff} determined by the vacuum copy-density functional. This extension is an auxiliary finite-density sector with its own variational constants. The primitive algebra, endpoint denominator, neutral generator, receiver inverse map, electroweak prediction ledger, and hydrodynamic likelihood have independent finite dependency graphs.

22. Prediction and Exclusion Hierarchy

The exclusion map is stratified by layer. The receiver layer has exclusion channels through absence of a six-cell local contour, exclusion by leakage-law curvature, no distance collapse, no amplitude collapse, or nonuniversal inverse coefficients. The spectral layer has exclusion channels through a visible finite algebra outside the Morita class to the primitive direct sum, endpoint transport not selecting $q = 14$, absence of the PMNS seed angle, wrong sign of J_{CP}^{ℓ}, or a neutral mass sum incompatible with the generated D_F^{ν}. Each prediction layer carries an explicit exclusion channel and dependency graph.

 doi:10.20944/preprints202604.0323.v5

The resulting exclusion map is therefore stratified:

$$\text{receiver exclusion} \Rightarrow \text{linear closure false}, \tag{84}$$

$$\text{endpoint exclusion} \Rightarrow \text{Weyl-family lift false}, \tag{85}$$

$$\text{neutral-generator exclusion} \Rightarrow \text{neutral spectral branch false}, \tag{86}$$

$$\text{prediction exclusion} \Rightarrow \text{threshold implementation incomplete}. \tag{87}$$

This distinction keeps auxiliary threshold and reconstruction material separate from the premises of the main theorem.

23. Primitive Closure Functional

The primitive principle can be represented variationally. Let Π_R denote the receiver projection and let I denote copy opposition. For a finite candidate $(\mathcal{A}, \mathcal{H}, D, J, \Gamma)$, define the closure penalty

$$\begin{aligned}\mathfrak{C}(\mathcal{A}, D) = \alpha\|\Pi_R[D, \mathcal{A}](1-\Pi_R)\|^2 + \beta\|I^2 - 1\|_{\mathrm{fp}}^2 + \gamma\|T_{\mathrm{end}} - Q\|_{\mathbb{Z}_3}^2 \\ + \delta\sum_{a,b}\|[[D, a], JbJ^{-1}]\|^2 + \eta\, N_{\mathrm{spec}},\end{aligned} \tag{88}$$

where the first term penalizes receiver leakage outside the declared support, the second enforces fixed-point-free opposition, the third enforces forward endpoint orientation, the fourth is first-order opposite locality, and the last counts quotient-null spectators. The primitive closure is the finite candidate of minimal $\mathfrak{C}$ among semisimple real finite algebras with nonzero receiver current. This functional form makes explicit why the constraints are Euler–Lagrange components of the primitive closure functional. They are the Euler–Lagrange projections of a single finite closure requirement.

In the zero-penalty sector the algebraic consequences are exactly those used in the classification theorem. A real central carrier has no continuous oriented phase and therefore does not satisfy the phase-current part of the variational problem. A complex central carrier does. A real two-dimensional opposition module represents an involution while the closure requires the antiunitary pseudoreal opposition with square -1. A quaternionic carrier does. A two-dimensional complex endpoint module does not carry the irreducible clock-shift pair of $\mathbb{Z}_3$. A three-dimensional complex module can. Tensor products of the primitive carriers increase the first-order penalty because primitive closure contains no additional superselection factor.

24. Detailed Receiver-Side Reconstruction Protocol

The receiver reconstruction protocol uses five independent quantities. First, the two zero-momentum eigenvalues give $\bar{E}_0$ and G_0. Second, the two branch curvatures give $\bar{C}$ and C_G. Third, the early-time visible leakage amplitude gives $A = m^2/G_0^2$. The coefficients are then recovered by (12). Measurement redundancy comes from the time dependence of the leakage law: once m, Δ, and v are reconstructed, the frequency Ω_k and amplitude $(m + vk^2)^2/\Omega_k^2$ are fixed simultaneously at several momenta.

The null branch is a receiver-relative null sector defined by the selected projector. If the receiver projector is changed, the visible/null split changes. This is a strength of the operational formulation: it prevents the formalism from assigning ontology to an unmeasured sector. The spectral closure enters only when one asks which finite microscopic algebra can generate a family of receiver projectors and finite Dirac blocks compatible with the quotient.

25. Detailed Gauge-Exchange Construction

The endpoint ring sector is a compact link theory on the certified contour. For each oriented edge $j \to j+1$, assign a link variable

$$U_{j,j+1} = \exp\{iA_j\} \in U(3), \tag{89}$$

 doi:10.20944/preprints202604.0323.v5

acting on the endpoint shield. Gauge covariance under $g_j \in U(3)$ is

$$U_{j,j+1} \mapsto g_j U_{j,j+1} g_{j+1}^{-1}. \tag{90}$$

The spoke sector couples opposition-related sites. Its minimal compact covariance is quaternionic and gives the $SU(2)$ doublet action. The central phase carrier supplies $U(1)$. Imposing unimodularity removes the redundant common determinant. The finite quotient therefore reproduces the observed product form of the gauge group from the finite quotient itself.

The same construction explains why the colour factor is endpoint-based rather than inserted by hand. The irreducible shield of the three endpoint classes is $M_3(\mathbb{C})$. Its inner automorphisms contain $PU(3)$, and after unimodularity the non-Abelian part is $SU(3)$. The pseudoreal opposition fibre supplies the weak $SU(2)$, and the complex phase line supplies hypercharge after unimodular mixing. These roles are distinct; exchanging them would either destroy endpoint irreducibility or fail the pseudoreal opposition condition.

26. Logical Architecture of the Closure

The full closure has four layers. Layer I is operational: copy time, validator selection, receiver shell, two-channel normal form, leakage, inverse map, and reduced rest-gap-time extraction. Layer II is finite algebraic: receiver quotient, primitive closure, block classification, first-order locality, unimodular gauge quotient, and chiral module. Layer III is spectral-flavour: endpoint denominator, Weyl-family holonomies, PMNS seed, CKM prediction, neutral Majorana matrix, and finite Dirac generator. Layer IV is empirical: receiver signatures, PMNS angle, CP branch, mass sum, copy-curvature ratio, electroweak prediction tables, and platform-independent exclusion.

Each layer supplies a distinct invariant and has an explicit proof dependency. The receiver layer gives observability but not the ultraviolet algebra. The algebraic layer gives the finite representation but not the time-domain receiver protocol. The flavour layer gives strong finite numerical targets but must be tied to the endpoint quotient. The empirical layer separates denominator predictions, finite-threshold predictions, and operational reconstructions. The receiver, spectral, gauge, flavour, electroweak, and hydrodynamic layers are treated with explicit proof dependencies and exclusion channels.

27. Completeness Checks against Finite Alternatives

The primitive closure is accompanied by a finite weakening test. Each clause of the closure principle removes a distinct class of countermodels. If receiver distinguishability is dropped, arbitrary central summands survive with no altering any receiver amplitude. If fixed-point-free opposition is dropped, a three-cycle can carry endpoint transport but does not carry the visible/null copy split. If endpoint orientation is dropped, fixed and inverse endpoint actions survive and the sign of the CP branch is no longer determined. If opposite first-order locality is dropped, tensor products of primitive carriers generate mixed commutators that are receiver-visible but not generated by the certified contour. If spectator removal is dropped, the classification ceases to be primitive because silent direct summands may be appended freely.

These alternatives are finite countermodels. The supplementary data file `primitive_closure_countermodels.csv` records the weakening, the surviving candidate, and the algebraic exclusion mode. The classification theorem is therefore read in the following strong form: among semisimple finite real involutive algebras with nonzero receiver current, the only primitive zero-penalty representative carrying continuous phase, pseudoreal opposition, irreducible three-endpoint transport, and opposite locality is

$$\mathbb{C} \oplus \mathbb{H} \oplus M_3(\mathbb{C}). \tag{91}$$

Additional summands either introduce extra receiver-visible currents, violate one of the primitive transport requirements, or are quotient-null spectators. This form is independent of presentation:

 doi:10.20944/preprints202604.0323.v5

replacing generators by a Morita-equivalent presentation does not change the receiver quotient, the opposite representation, or the endpoint clock-shift irreducibility class.

28. Unitary Charged-Flavour Exposure

The charged flavour layer is sharpened by replacing the hierarchy-only CKM prediction with an explicitly unitary endpoint matrix. Let

$$\lambda = \sin\frac{\pi}{14}, \qquad s_{12}^q = \lambda, \qquad s_{23}^q = \sqrt{\frac{2}{3}}\lambda^2, \qquad s_{13}^q = \frac{\lambda^3}{2\sqrt{2}}, \qquad \delta_q = \arccos\frac{1}{\sqrt{7}}. \tag{92}$$

The constants in (92) are endpoint quantities: λ is the primitive denominator seed; $\sqrt{2/3}$ is the two-sheet amplitude normalized by the three endpoint classes; $1/(2\sqrt{2})$ is the half-turn amplitude over the binary opposition cube; and $\arccos(1/\sqrt{7})$ is the primitive seven-denominator CP orientation. The charged mixing matrix is

$$V_q = R_{23}(s_{23}^q)R_{13}(s_{13}^q, \delta_q)R_{12}(s_{12}^q). \tag{93}$$

By construction $V_q^\dagger V_q = \mathbf{1}$ up to numerical precision. The audit file `ckm_unitary_matrix.csv` gives all complex entries, and `flavour_precision_audit.csv` gives the derived invariants. The CKM layer is a unitary charged-module prediction with endpoint origin and propagated uncertainty for each coefficient. The PMNS layer remains the denominator-level exposure through $\theta_{13}^{\mathrm{PMNS}} = \pi/21$ and the neutral CP orientation.

29. Electroweak Prediction Covariance

The electroweak prediction layer is represented by the finite map

$$X_a = X_a^{(0)} \exp[-C_a^{\mathrm{fin}}/(16\pi^2)], \qquad X_a \in \{v, g_1, g_2, \lambda_H, M_W, M_Z, m_H\}. \tag{94}$$

Let C_{EW} be the vector of finite Casimir contractions and Σ_C its Hessian covariance. The propagated theory covariance is

$$\Sigma_X = J_{X,C}\Sigma_C J_{X,C}^T, \qquad (J_{X,C})_{ab} = -X_a\delta_{ab}/(16\pi^2). \tag{95}$$

The supplementary file `electroweak_prediction_ledger.csv` records primitive values, finite Casimir contractions, finite-threshold predictions, theory covariance, reference values, and normalized residuals. The electroweak sector is therefore evaluated as a predictive finite-threshold layer of the completed receiver–spectral generator.

30. Hydrodynamic Likelihood and Rest-Gap Identifiability

The rest-gap protocol is written as an identifiable likelihood rather than as a curve-reading prescription. For distances L_i, thresholds η_j, and measured times T_{ij}, use

$$T_{ij} = \frac{L_i}{c_{\mathrm{eff}}} + b_0 + b_\eta(\eta_j - \eta_0) + \frac{b_L}{L_i} + \epsilon_{ij}, \qquad \epsilon \sim N(0, \Sigma_T). \tag{96}$$

The identifiable rest parameter is the profiled intercept b_0, and the extracted mass is

$$m_{\mathrm{eff}} = \frac{\hbar}{b_0 c_{\mathrm{eff}}^2}. \tag{97}$$

The protocol requires distance collapse, amplitude collapse, leakage-contamination control, positive Fisher information for b_0, and stability of m_{eff} under front subtraction. The audit file `hydrodynamic_likelihood_audit.csv` records these conditions. The hydrodynamic/rest-gap layer is therefore a falsifiable reconstruction scheme with explicit covariance, Fisher identifiability, and leakage-bias control.

 doi:10.20944/preprints202604.0323.v5

31. Extended Derivations of the Precision Closure

This section records the derivational chain in a form that can be read independently of the supplementary files. The finite closure is not introduced as a numerical ansatz. It is a sequence of constraints, quotients, transports, and finite traces. The order of operations is part of the construction: receiver quotient precedes finite block selection; finite block selection precedes endpoint lifting; endpoint lifting precedes flavour and threshold transport.

31.1. From Primitive Closure to Finite Blocks

Let $\mathcal{A}$ be a finite involutive real algebra acting faithfully on $\mathcal{H}_F$ before receiver quotient. Write the Wedderburn decomposition as

$$\mathcal{A} \simeq \bigoplus_{\alpha} M_{n_\alpha}(\mathbb{K}_\alpha), \qquad \mathbb{K}_\alpha \in \{\mathbb{R}, \mathbb{C}, \mathbb{H}\}. \tag{98}$$

The primitive closure tests each simple summand against four receiver-visible conditions. First, an oriented phase carrier must distinguish endpoint phases after quotient; this excludes purely real central blocks. Second, the opposition carrier must implement a fixed-point-free antilinear operation; this selects the pseudoreal quaternionic block. Third, endpoint shielding must act irreducibly on three quotient classes; this selects $M_3(\mathbb{C})$. Fourth, primitive locality excludes tensor products of these three carriers as new primitive summands.

Proposition 31.1 (Finite block uniqueness)**.** *The smallest receiver-visible algebra satisfying oriented phase distinction, fixed-point-free opposition, irreducible three-endpoint shielding, and first-order opposite locality is*

$$\mathcal{A}_F \simeq \mathbb{C} \oplus \mathbb{H} \oplus M_3(\mathbb{C}). \tag{99}$$

Proof. The complex block is the minimal finite algebra with a nontrivial oriented centre. The real block $\mathbb{R}$ has no oriented complex phase, and a higher complex matrix block contains a reducible phase carrier once quotient-null multiplicities are removed. The opposition block must carry a pseudoreal two-dimensional complex representation, hence its minimal real algebra is $\mathbb{H}$. A complex two-dimensional block cannot support the required antilinear square without an additional conjugate copy, which is quotient-null under receiver opposition. The endpoint block must act irreducibly on three classes. The minimal complex algebra acting irreducibly on a three-dimensional complex endpoint space is $M_3(\mathbb{C})$. Direct sums are allowed because the receiver distinguishes phase, opposition, and endpoint sectors; tensor products are excluded by first-order opposite locality because they introduce mixed commutators visible to the receiver quotient. The quotient by null spectators removes duplicate summands. The stated direct sum is therefore minimal and unique in the primitive class. □

31.2. Endpoint Denominator as an Explicit Action

Let $C_6 = \mathbb{Z}/6\mathbb{Z}$ and let $I(j) = j + 3$. The endpoint classes are $[0], [1], [2]$ in $C_6/I \simeq \mathbb{Z}_3$. The half-turn lift with denominator $q = 2r$ acts by

$$T_r[j] = [j + r] \quad \text{on } \mathbb{Z}_3. \tag{100}$$

The three possible congruence classes are

$$r \equiv 0 \pmod 3 : [j] \mapsto [j], \qquad r \equiv 1 \pmod 3 : [j] \mapsto [j+1], \qquad r \equiv 2 \pmod 3 : [j] \mapsto [j-1]. \tag{101}$$

The primitive orientation selects the forward generator, hence $r \equiv 1 \pmod 3$. Opposition separation requires r odd, receiver faithfulness requires $\gcd(r, 6) = 1$, and proper flavour lifting requires $q > 6$. The first integer satisfying these conditions is $r = 7$, so $q = 14$.

 doi:10.20944/preprints202604.0323.v5

Table 10. Endpoint-denominator sieve in the first nontrivial range.

r	$q = 2r$	r odd	$r \equiv 1 \pmod 3$	$\gcd(r,6) = 1$	admissible
1	2	yes	yes	yes	no, below proper lift
3	6	yes	no	no	no
5	10	yes	no	yes	no
7	14	yes	yes	yes	yes
9	18	yes	no	no	no
11	22	yes	no	yes	no
13	26	yes	yes	yes	later branch

31.3. CKM Matrix Entry Formulae

With $s_{ij} = \sin\theta_{ij}$ and $c_{ij} = \cos\theta_{ij}$, the generated CKM matrix is

$$V = \begin{pmatrix} c_{12}c_{13} & s_{12}c_{13} & s_{13}e^{-i\delta} \\ -s_{12}c_{23} - c_{12}s_{23}s_{13}e^{i\delta} & c_{12}c_{23} - s_{12}s_{23}s_{13}e^{i\delta} & s_{23}c_{13} \\ s_{12}s_{23} - c_{12}c_{23}s_{13}e^{i\delta} & -c_{12}s_{23} - s_{12}c_{23}s_{13}e^{i\delta} & c_{23}c_{13} \end{pmatrix}. \tag{102}$$

Substituting the finite charged coordinates gives the matrix in (68). The Jarlskog invariant is

$$J = c_{12}c_{23}c_{13}^2 s_{12}s_{23}s_{13}\sin\delta. \tag{103}$$

The derivatives needed for covariance propagation are

$$\frac{\partial s_{12}}{\partial \chi_{12}} = \frac{s_{12}}{16\pi^2}, \qquad \frac{\partial s_{23}}{\partial \chi_{12}} = \frac{2s_{23}}{16\pi^2}, \qquad \frac{\partial s_{13}}{\partial \chi_{12}} = \frac{3s_{13}}{16\pi^2}, \tag{104}$$

$$\frac{\partial s_{23}}{\partial \chi_{23}} = \frac{s_{23}}{16\pi^2}, \qquad \frac{\partial s_{13}}{\partial \chi_{13}} = \frac{s_{13}}{16\pi^2}, \qquad \frac{\partial \delta}{\partial \chi_{\delta}} = \frac{1}{16\pi^2}. \tag{105}$$

The derivatives of c_{ij} are obtained from $\partial c_{ij} = -(s_{ij}/c_{ij})\partial s_{ij}$. Combining these formulae gives the Jacobian used in the CKM covariance file.

31.4. Electroweak Threshold Algebra

The electroweak finite-threshold layer is a diagonal transport on the vector

$$X = (v, g_1, g_2, \lambda_H, M_W, M_Z, m_H). \tag{106}$$

For $C = (C_v, C_{g_1}, C_{g_2}, C_\lambda, C_W, C_Z, C_H)$,

$$\log X = \log X^{(0)} - \frac{C}{16\pi^2}. \tag{107}$$

Thus

$$\frac{\partial X_a}{\partial C_b} = -\frac{X_a}{16\pi^2}\delta_{ab}, \qquad \frac{\partial \log X_a}{\partial C_b} = -\frac{1}{16\pi^2}\delta_{ab}. \tag{108}$$

The finite Hessian covariance is transported by this Jacobian. The table below records the dimensionless contractions and relative prediction widths.

 doi:10.20944/preprints202604.0323.v5

Table 11. Electroweak precision covariance obtained from finite threshold transport.

Observable	Casimir	Prediction	Absolute sigma	Relative sigma
v	0.596491	246.2201	0.0300	1.22×10^{-4}
g_1	1.622222	0.349939984	5.0×10^{-5}	1.43×10^{-4}
g_2	0.440476	0.652830158	5.0×10^{-5}	7.66×10^{-5}
λ_H	2.222222	0.129070523	1.2×10^{-4}	9.30×10^{-4}
M_W	derived	80.369701	0.0060	7.47×10^{-5}
M_Z	derived	91.188052	0.0030	3.29×10^{-5}
m_H	derived	125.098088	0.0300	2.40×10^{-4}

31.5. Neutral Matrix Entries

The neutral Majorana matrix is symmetric by construction. Its entries are generated by

$$(M_\nu)_{ij} = m_1 \overline{U_{i1} U_{j1}} + m_2 \overline{U_{i2} U_{j2}} + m_3 \overline{U_{i3} U_{j3}}. \tag{109}$$

The six independent entries determine the Takagi spectrum. The supplementary file `neutral_Mnu_generated_eV.csv` lists all entries, while `takagi_audit.csv` verifies that the singular values coincide with the ladder in (42). The finite Dirac block D_F^ν doubles the spectrum with signs, hence its nonzero eigenvalues are $\pm m_i$.

31.6. Hydrodynamic Likelihood

Let t_i be receiver threshold times recorded at distances L_i and source amplitudes A_i. The branch-wise hydrodynamic model is

$$t_i = \alpha L_i + b_0 + A_i \beta + \varepsilon_i, \qquad \varepsilon_i \sim N(0, \sigma_i^2), \tag{110}$$

with leakage-corrected covariance $W = \mathrm{diag}(\sigma_i^{-2}) + W_{\mathrm{leak}}$. The intercept estimator is

$$\widehat{b}_0 = (e_0^T X^T W X)^{-1} e_0^T X^T W t, \tag{111}$$

where $X = (L, 1, A)$ and e_0 selects the intercept coordinate. The receiver mass estimator is

$$\widehat{m} = \frac{\hbar}{\widehat{b}_0 c_{\mathrm{eff}}^2}, \qquad \sigma_m = \frac{\hbar}{c_{\mathrm{eff}}^2 \widehat{b}_0^2} \sigma_{b_0}. \tag{112}$$

Branch stability is assessed by deleting distance and amplitude blocks and recomputing $\widehat{b}_0$. The reconstruction is accepted when all resampled intercepts remain inside the declared finite covariance envelope.

32. Integrated Precision Architecture

The construction now contains four mutually constraining numerical layers. The first is algebraic: the finite algebra, unimodular quotient, and anomaly-free chiral module are fixed by primitive closure. The second is endpoint-arithmetic: the denominator $q = 14$ follows from explicit transport on the three endpoint classes and the primitive holographic ground condition. The third is finite-dynamical: neutral, CKM, and electroweak precision outputs are generated by operator trace quotients of the finite generator. The fourth is receiver-operational: hydrodynamic rest-gap reconstruction tests whether the receiver propagation law is visible in distance- and amplitude-resolved data.

The main advantage of this organization is that no single numerical layer is allowed to redefine the finite algebra. Algebra comes first, then denominator, then finite generator, then observable transport. Conversely, every observable layer can exclude the construction. If the endpoint denominator is not fourteen, the PMNS target and charged endpoint traces change. If the finite operator trace quotients do not reproduce the electroweak precision ledger, the finite gauge-scalar transport is excluded. If the CKM matrix is not unitary under the generated angles and phase, the charged endpoint construction

 doi:10.20944/preprints202604.0323.v5

is excluded. If the receiver rest-gap intercept is not stable under distance and amplitude resampling, the receiver propagation layer is excluded.

32.1. Observable Hierarchy

The quantities in the manuscript are organized into four classes. Class I contains theorem-level structures: the quotient contour, finite algebra, unimodular gauge quotient, chiral matter module, and endpoint denominator. Class II contains finite precision predictions: PMNS, CKM, neutral masses, and electroweak threshold outputs. Class III contains receiver reconstructions: hydrodynamic intercepts, rest-gap mass estimators, leakage controls, and integer-core residuals. Class IV contains exclusion diagnostics: alternative finite blocks, endpoint-denominator candidates, covariance-inconsistent electroweak contractions, and unstable rest-gap reconstructions. The supplementary data are arranged in the same order.

32.2. Precision Reproducibility

All numerical claims in Class II are generated by the reproducibility scripts contained in `supplement/code/`. The script `build_precision_predictions.py` regenerates the CKM precision matrix, electroweak threshold ledger, operator trace quotients, covariance files, and summary pulls. The neutral matrices and receiver reconstruction ledgers are supplied as data files and are directly inspected by the audit script. A clean run produces the files listed in the supplementary data index without requiring external data downloads.

32.3. Acceptance and Exclusion Criteria

The finite closure is assessed by sector-specific criteria. Algebraic closure requires absence of a receiver-visible finite block outside $\mathbb{C} \oplus \mathbb{H} \oplus M_3(\mathbb{C})$ under the primitive closure principle. Endpoint closure requires the primitive holographic ground denominator to remain uniquely $q = 14$. PMNS closure requires $\theta_{13}^{\mathrm{PMNS}} = \pi/21$ and the negative sign of the leptonic Jarlskog invariant. CKM closure requires a unitary matrix with the reported angle and phase covariance. Electroweak closure requires the seven finite-threshold pulls to remain within the propagated finite-theory covariance. Hydrodynamic closure requires stable branchwise rest-gap reconstruction under distance, amplitude, leakage, and threshold resampling.

32.4. Data-Package Structure

The submission package contains the manuscript, the supplementary information, source files, figures, and a single supplement directory. The directory `supplement/data/` contains the finite matrices and ledgers. The directory `supplement/code/` contains the reproducibility scripts. The directory `figures/` contains vector and high-resolution raster figures used by the manuscript. This organization is intended to make the derivation auditable without inserting source-management material into the article itself.

33. Sector-By-Sector Reproducibility Formulae

The finite closure is reproducible because each numerical sector is governed by a closed map from a small set of primitive quantities. This section records those maps in a compact form.

33.1. Receiver Sector

For the two-channel receiver Hamiltonian

$$H_R = \mu \mathbf{1} + \nu \sigma_y + m \sigma_z + \kappa \sigma_x + \Delta \mathbf{1}_{\mathrm{null}}, \tag{113}$$

the receiver-visible splitting is

$$\Omega = \sqrt{m^2 + \kappa^2 + \nu^2}. \tag{114}$$

 doi:10.20944/preprints202604.0323.v5

The transition probability in the visible two-level sector is

$$P_{1\to 2}(t) = \frac{\kappa^2 + \nu^2}{\Omega^2} \sin^2(\Omega t), \tag{115}$$

and the receiver-null leakage channel contributes only through the quotient-visible leakage invariant

$$\Lambda_R(t) = \|P_R e^{-itH} P_N\|^2. \tag{116}$$

The inverse reconstruction uses the measured oscillation frequency, visibility contrast, phase shift, diagonal imbalance, and null leakage amplitude to recover $(\mu, \kappa, m, \Delta, \nu)$. The supplementary file `receiver_inverse_example.csv` gives a numerical instance.

33.2. Gauge and Anomaly Sector

The unimodular reduction of $\mathbb{C} \oplus \mathbb{H} \oplus M_3(\mathbb{C})$ gives

$$\frac{U(1) \times SU(2) \times U(3)}{U(1)_{\text{unimodular}}} \simeq \frac{U(1)_Y \times SU(2) \times SU(3)}{\mathbb{Z}_6}. \tag{117}$$

For one generation the hypercharges satisfy

$$6Y_Q + 2Y_L = 0, \qquad 3(2Y_Q - Y_u - Y_d) + (2Y_L - Y_e) = 0, \tag{118}$$

with solution

$$Y_Q = \frac{1}{6}, \quad Y_u = \frac{2}{3}, \quad Y_d = -\frac{1}{3}, \quad Y_L = -\frac{1}{2}, \quad Y_e = -1. \tag{119}$$

The cubic and mixed anomaly sums vanish:

$$\sum_{\text{left}} Y^3 - \sum_{\text{right}} Y^3 = 0, \qquad \sum_{\text{doublets}} Y = 0, \qquad \sum_{\text{triplets}} Y = 0. \tag{120}$$

These identities are representation-level consistency equations of the finite closure.

33.3. Flavour Sector

The lepton and quark matrices are both generated by endpoint holonomies, but they expose different finite modules. The lepton matrix uses the denominator-level angle $\pi/21$, while the quark matrix uses finite trace-corrected charged coordinates. The common origin is visible in the pair

$$\theta_{13}^{\text{PMNS}} = \frac{1}{3}\frac{2\pi}{14}, \qquad \lambda_q = \sin\frac{\pi}{14} \exp\Big(\frac{\chi_{12}}{16\pi^2}\Big). \tag{121}$$

Thus the lepton exposure is denominator-exact and the quark exposure is denominator-plus-trace. The two sectors test the same endpoint arithmetic at different levels of the finite module.

33.4. Electroweak Sector

The electroweak primitive quantities can be written in a single vector equation,

$$X^{(0)} = \left(\sqrt{8} E_P e^{-4\pi^2}, \frac{1}{2\sqrt{2}}, \sqrt{\frac{3}{7}}, \frac{\pi}{24}, \frac{1}{2} g_2^{(0)} v_0, \frac{1}{2} v_0 \sqrt{(g_1^{(0)})^2 + (g_2^{(0)})^2}, \sqrt{2\lambda_H^{(0)}} v_0 \right). \tag{122}$$

Threshold transport is the diagonal exponential map

$$X = \exp\left[-\frac{1}{16\pi^2} \operatorname{diag}(C_v, C_{g_1}, C_{g_2}, C_\lambda, C_W, C_Z, C_H) \right] X^{(0)}. \tag{123}$$

 doi:10.20944/preprints202604.0323.v5

The precision comparison is therefore reproducible from $X^{(0)}$, the finite Casimir vector, and the covariance file.

33.5. Neutral Sector

The neutral sector combines the Planck scale, the four-sheet saddle, endpoint holonomy, trace compression, and endpoint volume. The three scales are

$$m_3 = E_P(\sqrt{8}e^{-4\pi^2})^2 e^{3\pi}, \qquad m_2 = \frac{m_3}{\sqrt{34}}, \qquad m_1 = \frac{m_2}{6\pi^2}. \tag{124}$$

The Majorana matrix is obtained from the generated PMNS matrix; its Takagi factorization returns precisely the ladder. This closes the neutral chain from finite constants to matrix entries to singular values.

34. Detailed Observable Tables

Table 12. End-to-end observable ledger in the main manuscript.

Sector	Observable	Generated value	Generator map	Data file
Algebra	$\mathcal{A}_F$	$\mathbb{C} \oplus \mathbb{H} \oplus M_3(\mathbb{C})$	primitive closure	block classification
Endpoint	q	14	$r \equiv 1 \pmod 3$, $q = 2r$	q admissibility
PMNS	θ_{13}	8.57142857°	$\pi/21$	pmns comparison
PMNS	J^{ℓ}_{CP}	-0.03355795	unitary invariant	flavour audit
Neutral	$\sum m_i$	0.072810131 eV	Takagi spectrum	takagi audit
CKM	θ^q_{12}	12.973478°	finite trace coordinate	CKM precision
CKM	δ_q	68.7000°	CP trace coordinate	CKM precision
CKM	J^q_{CP}	3.189591×10^{-5}	unitary invariant	CKM precision
EW	v	246.2201 GeV	threshold transport	electroweak ledger
EW	g_1	0.349939984	threshold transport	electroweak ledger
EW	g_2	0.652830158	threshold transport	electroweak ledger
EW	λ_H	0.129070523	threshold transport	electroweak ledger
EW	M_W	80.369701 GeV	threshold transport	electroweak ledger
EW	M_Z	91.188052 GeV	threshold transport	electroweak ledger
EW	m_H	125.098088 GeV	threshold transport	electroweak ledger
Receiver	rest-gap intercept	branch dependent	hydrodynamic likelihood	rest-gap audit
Receiver	K_{copy}	1	paired curvature onset	curvature audit
Endpoint echo	phase maxima	$\pi/21 + 2\pi a/3$	receiver-null boundary channel	Online Resource 3
Endpoint echo	period ratio	3/2	$q_v/q = 21/14$	Online Resource 3
Endpoint echo	onset	quadratic in ε	odd boundary-to-Majorana perturbation	Online Resource 3

 doi:10.20944/preprints202604.0323.v5

35. Experimental Exposure

The model has several independent exposure channels. The denominator exposure is controlled by lepton mixing; the neutral exposure is controlled by absolute mass probes; the charged exposure is controlled by CKM unitarity and CP violation; the electroweak exposure is controlled by finite-threshold precision; and the receiver exposure is controlled by distance- and amplitude-resolved copy-time data. These channels are mathematically connected but statistically independent in their measurement procedures.

35.1. Lepton and Neutral Exposure

The lepton sector is exposed through $\theta_{13}^{\mathrm{PMNS}}$, the sign and magnitude of J_{CP}^{ℓ}, and the absolute mass sum. Improved long-baseline data test the CP-orientation sign, while cosmological and beta-decay channels test the absolute-mass branch. The finite construction specifies a normal ordering and a mass sum below current cosmological upper bounds.

35.2. Charged-Quark Exposure

The charged sector is exposed through a unitary matrix rather than through isolated matrix elements. The natural comparison object is the vector

$$(|V_{ud}|, |V_{us}|, |V_{ub}|, |V_{cb}|, |V_{tb}|, \delta_q, J_{CP}^{q}). \tag{125}$$

The covariance supplied with the manuscript propagates finite-generator uncertainty to this vector.

35.3. Electroweak Exposure

The electroweak sector is exposed through a seven-dimensional finite-threshold vector. Since the transport is multiplicative, the appropriate comparison is logarithmic:

$$\Delta_a = \log X_a - \log X_a^{\mathrm{ref}}. \tag{126}$$

The covariance in Δ_a is obtained by dividing the absolute covariance by the predicted values. This formulation is stable under units and avoids assigning special status to dimensional coordinates.

35.4. Receiver Exposure

Receiver exposure is platform-independent. A receiver experiment probes the operational layer without requiring a full finite Standard-Model realization. It tests the operational layer: copy-time thresholding, leakage separation, distance collapse, amplitude collapse, and rest-gap intercept stability. Positive receiver tests support the quotient structure; negative receiver tests exclude the operational premise independently of the particle-sector precision predictions.

35.5. Prospective Receiver-Null Endpoint Echo

Beyond comparison with oscillation, CKM, electroweak and absolute-mass data, the model predicts a receiver-null boundary-to-Majorana endpoint echo. The signal is generated when the primitive boundary atom is coupled to the real Takagi branch by a controlled perturbation supported on $P_\partial \oplus P_M$. The leading echo intensity obeys

$$\mathcal{E}_{\partial \to M}(t, \varepsilon) = \varepsilon^2 F(t; \mu_\partial, \mu_M) + O(\varepsilon^4), \tag{127}$$

with no zeroth-order signal and no linear intensity term. Its phase maxima are predicted at

$$\Theta_a = \frac{\pi}{21} + \frac{2\pi a}{3}, \qquad a = 0, 1, 2, \tag{128}$$

 doi:10.20944/preprints202604.0323.v5

and the neutral-to-oriented-lift period ratio is

$$\frac{T_\nu}{T_q} = \frac{21}{14} = \frac{3}{2}. \tag{129}$$

These quantities are not extracted from NuFIT global fits, DUNE design sensitivities, CKM fits, or electroweak reference values. They are prospective receiver signatures of the finite channel support. Online Resource 3 gives the derivation, exclusion controls, prediction ledger and a dimensionless numerical simulation used only to visualize the phase-satellite and quadratic-onset tests.

35.6. Endpoint-Echo Experimental Protocol

The endpoint echo is intended as a receiver experiment rather than as an additional oscillation-fit parameter. A minimal implementation requires four operational capabilities: preparation of the primitive boundary atom, controlled opening of the boundary-to-Majorana support, endpoint phase scanning, and receiver-front subtraction. Denote the measured echo power by $Y(t, \varphi, \varepsilon)$, where φ is the controllable endpoint phase and ε is the strength of the boundary-to-Majorana channel. The primary regression model is

$$Y(t, \varphi, \varepsilon) = Y_0(t) + \varepsilon^2 F(t)[1 + \kappa \cos\{3(\varphi - \pi/21)\}] + R(t, \varphi, \varepsilon), \tag{130}$$

with $R = O(\varepsilon^4) + O(\delta_{\text{leak}})$. The platform-dependent quantities are the envelope $F(t)$, the visibility κ, and the leakage residual δ_{leak}. The phase offset $\pi/21$, the threefold satellite spacing, the quadratic onset, and the ratio $T_\nu/T_q = 3/2$ are not platform parameters.

A minimal laboratory realization may be sought in a six-mode photonic ring or in an equivalent superconducting-mode network. The six modes implement the certified boundary contour, the antipodal coupling implements the copy opposition, three independently addressable phase shifters implement the endpoint quotient, and an auxiliary detunable mode implements the real fixed branch used for support removal. In such a platform ε is the calibrated boundary-to-auxiliary coupling, φ is the controlled endpoint phase, and Y is the integrated receiver power after subtraction of the front response. The theory does not identify the auxiliary mode with a new elementary particle; it predicts the receiver-null support signature that any admissible realization must display.

The null controls are fixed by support. With the channel closed, $\varepsilon = 0$, the background-subtracted echo vanishes:

$$Y(t, \varphi, 0) - Y_0(t) = 0. \tag{131}$$

With the Majorana fixed branch removed or detuned away from the support of $P_M V_{\partial M} P_\partial$, the same background-subtracted echo is absent to the declared leakage order:

$$Y_{\text{off}}(t, \varphi, \varepsilon) - Y_0(t) = O(\delta_{\text{leak}}). \tag{132}$$

A positive test therefore requires all four conditions

$$\partial_\varepsilon Y|_{\varepsilon=0} = 0, \quad \partial_\varepsilon^2 Y|_{\varepsilon=0} > 0, \quad \varphi_{\max} = \frac{\pi}{21} + \frac{2\pi a}{3}, \quad \frac{T_\nu}{T_q} = \frac{3}{2}, \tag{133}$$

within the independently reported phase, timing and leakage uncertainties. Failure of any one of the four conditions gives a layer-specific exclusion rather than a fit adjustment. This protocol turns the endpoint echo into a falsifiable receiver signature with an explicit null model and a fixed phase register.

36. Internal Consistency Checks

The final closure contains several algebraic consistency checks that do not depend on external numerical comparison. The first check is quotient stability: replacing the prequotient presentation of

 doi:10.20944/preprints202604.0323.v5

the finite algebra by a Morita-equivalent presentation leaves the receiver-visible algebra unchanged. The second check is opposite locality: the commutator $[[D_F, a], JbJ^{-1}]$ vanishes for primitive algebra elements after quotient-null summands are removed. The third check is unitary stability: the CKM and PMNS matrices generated from the endpoint coordinates obey exact unitarity before numerical rounding. The fourth check is Takagi stability: the singular values of M_ν are invariant under rephasing of the Majorana convention.

These checks are structural and are evaluated before electroweak or CKM reference comparison. They test whether the internal construction is well-defined before phenomenological comparison. The supplementary data include the finite matrices used in these checks, and the reproduction scripts verify the numerical invariants generated from them.

Table 13. Internal consistency checks used before phenomenological comparison.

Consistency check	Mathematical condition	Consequence
Quotient stability	$\mathcal{A}_0/\mathcal{N}_R$ is invariant under presentation change	observable algebra is presentation independent
Opposite locality	$[[D_F, a], JbJ^{-1}] = 0$	primitive tensor products are excluded
Unimodularity	trace of total finite gauge potential vanishes	hypercharge quotient is fixed
CKM unitarity	$V_{\mathrm{CKM}}^\dagger V_{\mathrm{CKM}} = \mathbf{1}$	charged mixing is a genuine unitary exposure
PMNS unitarity	$U_\ell^\dagger U_\ell = \mathbf{1}$	neutral Majorana matrix has a stable Takagi spectrum
Takagi stability	$U_T^T M_\nu U_T = \mathrm{diag}(m_i)$	singular values equal the neutral ladder
Hydrodynamic identifiability	Fisher matrix for (α, b_0, β) is nonsingular	rest-gap mass estimator is defined

37. Methods and Data Availability

The submission contains four online resources. Online Resource 1 is the extended supplementary information for primitive closure, finite-block classification, receiver reconstruction, anomaly cancellation, precision ledgers, and validation protocols. Online Resource 2 is the complete Takagi and neutral-constant derivation, with explicit projectors, trace calculations, determinant, endpoint residue, primitive angle theorem, and reproduction formulas. Online Resource 3 is the complete prediction ledger and prospective receiver-null endpoint-echo derivation. Online Resource 4 contains code and machine-readable audit data. The code regenerates the CKM precision files, electroweak threshold files, endpoint-denominator tables, block-classification tables, Majorana matrices, neutral Dirac block, Takagi audit, receiver prediction files, comparison files, and logical-status registers.

Supplementary Materials: The following supporting information can be downloaded at the website of this paper posted on Preprints.org.

Author Contributions: Mohamed Sacha developed the theoretical framework, prepared the calculations, generated the submission files, and wrote the manuscript and supplementary information.

Funding: No external funding was received for this work.

Acknowledgments: The author acknowledges independent theoretical discussions on quantum information, finite spectral geometry, and neutrino phenomenology.

Conflicts of Interest: The author declares no competing interests.

References

1. C. W. Helstrom, *Quantum Detection and Estimation Theory*, Academic Press, 1976.
2. A. Connes, *Noncommutative Geometry*, Academic Press, 1994.

 doi:10.20944/preprints202604.0323.v5

3. A. H. Chamseddine and A. Connes, The spectral action principle, *Communications in Mathematical Physics* **186**, 731–750 (1997).
4. A. Connes and M. Marcolli, *Noncommutative Geometry, Quantum Fields and Motives*, American Mathematical Society, 2008.
5. J. W. Barrett, A Lorentzian version of the noncommutative geometry of the Standard Model of particle physics, *Journal of Mathematical Physics* **48**, 012303 (2007).
6. W. D. van Suijlekom, *Noncommutative Geometry and Particle Physics*, Springer, 2015.
7. E. Witten, An SU(2) anomaly, *Physics Letters B* **117**, 324–328 (1982).
8. L. Alvarez-Gaume and P. Ginsparg, The structure of gauge and gravitational anomalies, *Annals of Physics* **161**, 423–490 (1985).
9. K. Fujikawa, Path-integral measure for gauge-invariant fermion theories, *Physical Review Letters* **42**, 1195–1198 (1979).
10. S. Weinberg, *The Quantum Theory of Fields. Volume 1: Foundations*, Cambridge University Press, 1995.
11. M. E. Peskin and D. V. Schroeder, *An Introduction to Quantum Field Theory*, Westview Press, 1995.
12. Particle Data Group, Review of Particle Physics, *Physical Review D* **110**, 030001 (2024).
13. I. Esteban et al., NuFIT-6.0: updated global analysis of three-flavor neutrino oscillations, arXiv:2410.05380 (2024).
14. DUNE Collaboration, Deep Underground Neutrino Experiment (DUNE), Far Detector Technical Design Report, Volume II, arXiv:2002.03005 (2020).
15. Hyper-Kamiokande Proto-Collaboration, Hyper-Kamiokande Design Report, arXiv:1805.04163 (2018).
16. C. Rovelli, Relational quantum mechanics, *International Journal of Theoretical Physics* **35**, 1637–1678 (1996).
17. C. Rovelli, *Quantum Gravity*, Cambridge University Press, 2004.
18. H. Georgi and S. L. Glashow, Unity of all elementary-particle forces, *Physical Review Letters* **32**, 438–441 (1974).
19. M. B. Green, J. H. Schwarz and E. Witten, *Superstring Theory*, Vols. 1–2, Cambridge University Press, 1987.
20. J. Polchinski, *String Theory*, Vols. 1–2, Cambridge University Press, 1998.
21. J. D. Bekenstein, Black holes and entropy, *Physical Review D* **7**, 2333–2346 (1973).
22. G. ŕ Hooft, Dimensional reduction in quantum gravity, arXiv:gr-qc/9310026 (1993).
23. L. Susskind, The world as a hologram, *Journal of Mathematical Physics* **36**, 6377–6396 (1995).